

LEVEL II

NRL Report 8430

AD A092151

**Spatial Coherence Measurements and Evaluation
of a Noise Reduction Technique for Ambient Noise
from 0.3 to 40 Hz**

R. J. DINGER AND J. A. GOLDSTEIN

*Telecommunication Systems Technology Branch
Communications Sciences Division*

October 15, 1980



NAVAL RESEARCH LABORATORY
Washington, D.C.

Approved for public release; distribution unlimited.

**DTIC
ELECTE
NOV 26 1980**

DDC FILE COPY

80 11 25 034

UNCLASSIFIED

SECURITY CLASSIFICATION OF THIS PAGE (When Data Entered)

REPORT DOCUMENTATION PAGE		READ INSTRUCTIONS BEFORE COMPLETING FORM
1. REPORT NUMBER NRL Report 8430	2. GOVT ACCESSION NO. AD-A092151	3. RECIPIENT'S CATALOG NUMBER
4. TITLE (and Subtitle) SPATIAL COHERENCE MEASUREMENTS AND EVALUATION OF A NOISE REDUCTION TECHNIQUE FOR AMBIENT NOISE FROM 0.3 TO 40 HZ	5. TYPE OF REPORT & PERIOD COVERED Final report on one phase of a continuing NRL problem.	
7. AUTHOR(s) R. J. Dinger and J. A. Goldstein	8. CONTRACT OR GRANT NUMBER(s) 1011921021	
9. PERFORMING ORGANIZATION NAME AND ADDRESS Naval Research Laboratory Washington, DC 20375	10. PROGRAM ELEMENT, PROJECT, TASK AREA & WORK UNIT NUMBERS NRL Problem 74-0200-0-0, Task Area RR021-01-41, Program Element 67721N	
11. CONTROLLING OFFICE NAME AND ADDRESS (12) 68 171 100-100000	12. REPORT DATE October 15, 1980	
14. MONITORING AGENCY NAME & ADDRESS (if different from Controlling Office) (12) 15 Oct 80	13. NUMBER OF PAGES 59	
	15. SECURITY CLASS. (of this report) UNCLASSIFIED	
	16. DECLASSIFICATION/DOWNGRADING SCHEDULE	
16. DISTRIBUTION STATEMENT (of this Report) Approved for public release; distribution unlimited.		
17. DISTRIBUTION STATEMENT (of the abstract entered in Block 20, if different from Report)		
18. SUPPLEMENTARY NOTES		
19. KEY WORDS (Continue on reverse side if necessary and identify by block number) Ultra low frequency (ULF) Schumann resonances Extremely low frequency (ELF) SQUID Atmospheric noise Magnetic anomaly detection (MAD)		
20. ABSTRACT (Continue on reverse side if necessary and identify by block number) Measurements of the ambient magnetic field in the frequency range from 0.3 Hz to 40 Hz were made at a mid-latitude location in winter (China Lake, California) and an auroral location in summer (Tromsø, Norway). At each location two sensitive triaxial SQUID magnetometers were installed at sites whose separation was varied from 0.5 km to 15 km (in California) and from 0.5 km to 9.3 km (in Norway). Approximately two weeks of nearly continuous data were recorded at each location. Schumann resonances with a particularly high ratio of signal-to-instrument noise were (Continues)		

DD FORM 1473

1 JAN 73

EDITION OF 1 NOV 65 IS OBSOLETE
S/N 0102-014-6A01

UNCLASSIFIED

SECURITY CLASSIFICATION OF THIS PAGE (When Data Entered)

20. Abstract (Continued)

→ observed, with six orders of the resonances typically visible. Peaks attributed to wind-induced motion noise were observed in the spectra, particularly at the exposed China Lake sites. Prominent spikes were present in the spectra above about 10 Hz; except for several of these spikes that were traced to the tape recorder playback electronics, they are believed to represent genuine man-made ambient signals. Probable sources of the interference include 4-pole synchronous motor emissions, powerline subharmonics, and electrified railway or telephone ringing signal emissions. In California the coherence between the nominally parallel sensors at the two sites was relatively high (greater than 0.75) at all separations and showed definite peaks at the frequencies of the Schumann resonances. The coherence was highest at frequencies from about 5 Hz to 20 Hz, usually 0.9 or more. No structure in the coherence attributable to the effects of geological inhomogeneities was seen in the California data. The coherence between orthogonal sensors in both California and Norway was usually 0.25 or less and was highly variable. In Norway coherence at 9.3 km approached a value of 0.9 at the highest but showed structure that probably is associated with the conductivity anomaly caused by a nearby fjord.

An algorithm first described by Fowler, Smith, and Bostick (FSB) was investigated analytically for its ability to suppress the ambient noise by using frequency domain signal differencing. The FSB processing of the data consistently produced a difference signal whose noise spectral density was very near the SQUID magnetometer intrinsic noise except for a noticeable increase below 5 Hz. Seismic-induced motion noise in the SQUID sensors probably accounts for this increase in the processed difference below 5 Hz. The FSB processing typically produced a decrease of 30 to 40 dB or more compared with the spectral amplitude of the ambient noise.

The results reported here indicate that atmospheric and geomagnetic noise in the band from 0.3 to 40 Hz can be reduced essentially to the instrument noise level by using difference processing with two magnetometers.

Accession For	
NTIS GRA&I	<input checked="" type="checkbox"/>
DTIC TAB	<input type="checkbox"/>
Unannounced	<input type="checkbox"/>
Justification	
By	
Distribution/	
Availability Codes	
Dist	Avail and/or Special
A	

DTIC
ELECTE
NOV 26 1980
D

CONTENTS

SUMMARY	1
INTRODUCTION	2
SPATIAL CORRELATION AND NOISE REDUCTION	3
Introduction	3
Fowler, Smith and Bostick (FSB) Technique	4
Background	4
Coefficient Evaluation	5
Alternative Derivation of the Coefficients	8
Expected Noise Level of the Difference Signal Δ	10
DATA COLLECTION	11
DATA ANALYSIS TECHNIQUES	16
Spectral Analysis	17
Coherence Analysis	18
FSB Analysis	19
RESULTS	
Spectral Analysis Results	20
Coherence Results	27
California Data	33
Norway Data	33
FSB Processing Results	34
California Data	34
Norway Data	43
CONCLUSIONS AND RECOMMENDATIONS	46
ACKNOWLEDGMENTS	47
REFERENCES	47
APPENDIX A — Processed Difference Noise Level	49
APPENDIX B — The Effect of an Angular Misalignment Error ..	52

SPATIAL COHERENCE MEASUREMENTS AND EVALUATION OF A NOISE REDUCTION TECHNIQUE FOR AMBIENT NOISE FROM 0.3 TO 40 HZ

SUMMARY

Measurements of the ambient magnetic field in the frequency range from 0.3 Hz to 40 Hz have been made at a mid-latitude location in winter (China Lake, California) and an auroral location in summer (Tromsø, Norway). At each location two sensitive triaxial SQUID magnetometers were installed at sites whose separation varied from 0.5 km to 15 km (in California) and from 0.5 km to 9.3 km (in Norway). Approximately two weeks of nearly continuous data were recorded at each location. The data analysis in this report is concerned primarily with frequency domain investigations: spectral features in the recorded magnetometer signals are identified, the frequency-dependent spatial coherence is calculated for various combinations of sensor axes and its features analyzed, and a frequency domain signal differencing technique is assessed for its ability to suppress the ambient noise. The major effort was expended in analyzing and assessing the noise suppression technique. Our specific comments and conclusions regarding each area of the data analysis are as follows:

- *Ambient noise spectra.* Schumann resonances with a particularly high ratio of signal-to-instrument noise were observed. Six orders of the resonances were typically observed in the spectra. Significant peaks attributed to wind-induced motion noise were observed in the spectra particularly at the exposed China Lake sites. Prominent spikes were present in the spectra above about 10 Hz; except for several of these spikes that were traced to the tape recorder playback electronics, they are believed to represent genuine man-made ambient signals. Sources of the interference include 4-pole synchronous motor emissions, powerline subharmonics, and electrified railway or telephone ringing signal emissions.

- *Spatial Coherence.* In California the coherence between the nominally parallel sensors at the two sites was relatively high (greater than 0.75) at all separations and showed definite peaks at the frequencies of the Schumann resonances. The coherence was highest at frequencies from about 5 Hz to 20 Hz, usually 0.9 or more. No structure in the coherence attributable to the effects of geological inhomogeneities was seen in the California data. Larger separation distances than 15 km would be necessary to observe geological effects. A large decrease in the coherence at certain frequencies was noticeable for data contaminated by wind-induced motion noise. The coherence between orthogonal sensors in both California and Norway was usually 0.25 or less and was highly variable. The Norway coherence results revealed a surprisingly low coherence of about 0.5 between sensors assumed to be parallel at the 0.5 km separation. This low coherence, taken together with the difference processing results, can be explained in a consistent manner by postulating that the remote site magnetometer was inadvertently installed with the horizontal axes rotated by 30° . The coherence at 9.3 km approached a value of 0.9 at the highest but showed structure that we believe is associated with the conductivity anomaly caused by a nearby fjord.

Manuscript submitted May 19, 1980

• *Fowler-Smith-Bostick (FSB) Processing.* The FSB algorithm was first investigated analytically and an expression derived from the processed difference signal that aided in the interpretation of the processing. The FSB processing of the data consistently produced a difference signal whose noise spectral density was very near the SQUID magnetometer intrinsic noise except for a noticeable increase below 5 Hz. Seismic-induced motion noise in the SQUID sensors probably accounts for this increase in the processed difference below 5 Hz. The FSB processing typically produced a decrease of 10 to 30 dB in the difference spectral amplitude, compared with the simple first difference, and produced a decrease of 40 dB or more compared with the spectral amplitude of the ambient noise.

The results reported here indicate that atmospheric and geomagnetic noise in the band from 0.3 to 40 Hz can be reduced essentially to the instrument noise level by using difference processing with two magnetometers.

INTRODUCTION

This report is concerned with the measurement and characterization of naturally occurring ambient electromagnetic noise in the frequency range from 0.3 Hz to 40 Hz and with the evaluation of a technique to reduce the noise spectral density. The lower decade of this frequency range lies in the ultra low frequency (ULF, 0 to 3 Hz) band; noise in this band is generated by processes that occur in the magnetosphere and upper ionosphere. At frequencies above 3 Hz in the extremely low frequency (ELF, 3 to 3000 Hz) band, the noise is dominated by atmospheric impulses generated by near and distant lightning strokes. The study of noise in this frequency band and techniques for its mitigation is important for submarine magnetic anomaly detection (MAD) applications and for proposed ULF/ELF low data rate communication systems. Noise measurements are also of fundamental interest as a ground-based ionospheric/magnetospheric diagnostic technique and as a technique for geophysical exploration.

Approximately four weeks of nearly continuous recordings were taken at sites in California and Norway. At each site two triaxial superconducting quantum interference device (SQUID) magnetometers were used that were separated by distances varying between 0.5 km and 15 km. Because of the very large quantity of data collected, the emphasis in this report is on the analysis and interpretation of selected intervals of these recordings to determine frequency spectra and the frequency dependent spatial coherence function, and to evaluate a frequency domain noise cancellation technique; in short, frequency domain analysis is favored. A future report is planned that will examine the temporal characteristics of the recorded noise.

Although much observational data of atmospheric and ionospheric/magnetospheric noise exist in the literature (see Ref. 1 for a list of recent references), most of these data were taken with conventional loop-type antennas whose self-noise level has been demonstrated [2] to exceed often the average ambient noise level in the 0.3 to 40 Hz band, particularly in the 2 to 8 Hz portion of this band. Measurements with sensitive SQUID magnetometers have been reported by Fraser-Smith and Buxton [1,2] and Zimmerman and Campbell [3], but these measurements in each case were for one fixed site in one geographic location. The measurements reported here are the first of ambient noise and its spatial coherence taken

with SQUID magnetometers at dual sites. The coherence enhancement technique that we have chosen to use was first described by Fowler, Smith, and Bostick [4], who applied the method to coil magnetometer data gathered by them in a frequency range from 10^{-4} to 0.1 Hz. However, the remote reference magnetotelluric technique of Gamble, *et al* [5,6] has some resemblance to the processing techniques described in this report.

In the next section the various factors that affect the spatial coherence of 0.3 to 40 Hz noise are discussed, and an algorithm by which the apparent coherence can be enhanced is derived. The relationship of the algorithm to linear systems theory is demonstrated in order to assist in the interpretation of the processing results. Then details of the data collection effort are given. The next section discusses the various data analysis techniques for determining the spectra and the spatial coherences, and for investigating the coherence enhancement algorithm. An expression for the noise spectral density after the coherence enhancement technique is applied is derived. Next the results of the data analysis are given, and finally the conclusions of the study and recommendations for further work are reported.

SPATIAL CORRELATION AND NOISE REDUCTION

Introduction

Since the free space wavelengths in the 0.3 to 40 Hz range vary between 10³ Mm and 7.5 Mm, one might expect the noise fields to be highly correlated over very large distances. However, on the earth's surface high correlation exists over distances of only tens of kilometers, for the following reasons:

- The measurement sites, particularly for geomagnetic noise below several hertz, are necessarily in the complex near field of the sources;
- The sources can be dispersed, so that the wavefronts are not perfectly coherent;
- Inhomogeneous geology in the vicinity of the measurement sites can distort (or, from a different point of view, scatter) the incident noise fields, thereby lowering the correlation.

These decorrelating factors are all intrinsic properties of the noise fields themselves; of the three the last factor probably contributes the most to the lowering of the coherence. Two additional factors associated with the detection of the fields also cause an apparent lowering of the correlation:

- Misalignment or uncompensated motion of the presumed parallel vector sensors will lower the correlation;
- Intrinsic sensor noise can appreciably degrade the measured correlation if the signal to noise ratio is low.

The goal of a noise reduction technique is to enhance the apparent site-to-site spatial correlation by compensating in some manner for the decorrelating factors listed above. Of

more fundamental interest is the determination of the degree to which each of the listed factors contributes to the measured coherence. For example, separation of source and instrumental effects from geology effects would be important if spatial coherence surveys were to be applied to geophysical exploration. We have found, however, that separation of the factors is difficult to accomplish in measured data, a point to be discussed in detail later.

We now describe a technique first derived by Fowler, Smith, and Bostick [4] for enhancing the correlation. This technique was applied to all of our data and was extensively evaluated.

Fowler, Smith, and Bostick (FSB) Technique

Background

The FSB algorithm begins by forming a linear relationship (transfer function) between the three orthogonal magnetic field vector components measured at one receiver site (denoted the base site) and a single vector component at the other site (denoted the remote site) that is given by

$$\Delta(f) = R(f) - A(f)X(f) - B(f)Y(f) - C(f)Z(f), \quad (1)$$

where R is the Fourier transform (FT) of the sensor output of the remote site; X is the FT of one horizontal component of the base site; Y is the FT of the other orthogonal horizontal component of the base site; Z is the FT of the vertical component of the base site; Δ is the difference signal; A , B , and C are coefficients to be determined; and f is the frequency. The vector component R in general can be in any fixed arbitrary direction at the remote site, i.e., it is not assumed that the direction of R is in the same compass direction as X , Y , or Z at the base site. However, during the experimental measurements we usually attempted to align the three orthogonal sensors of the remote site SQUID magnetometer so that they were approximately parallel with the base site sensors. When we want to refer to one of these remote site sensors, we will use the notation R_x , R_y , and R_z , where the subscript denotes the axis at the base site that the remote site is nominally parallel to. See Fig. 1.

The coefficients A , B , and C express a linear frequency dependent relationship between the base and remote sites; they form what FSB call a "geology filter" in reference to the assumption that local inhomogeneities in the subsurface geology are the dominant contribution to the particular values of the coefficients.* In a MAD application the coefficients would be evaluated in the known absence of a perturbation signal at the remote site (the remote site is assumed to be the sensor attempting to detect a target). The coefficients thus determined would then be used to form the difference according to Eq. (1) at a later time;

*The use of three separate letters for these coefficients instead of a single subscripted variable leads to some awkwardness in the resulting equations. However, we choose to adopt the notation of FSB.

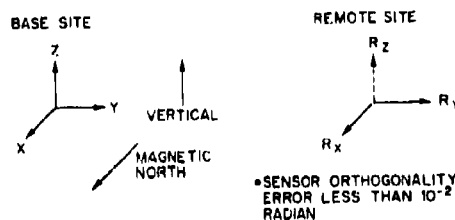


Fig. 1 — Geometry and notations for base and remote sites. The sensor R_x , although recorded part of the time, was not used in any of the data processing reported here.

because the value of $\Delta(f)$ is now, we expect, much less than $R(f)$, the anomaly signal would be enhanced (the implicit assumption is made that the base site is sufficiently far removed so that it does not detect the anomaly). In a geophysical exploration technique the specific structure of $A(f)$, $B(f)$, and $C(f)$ would be used to gain knowledge of the subsurface geology. The effectiveness of the FSB approach depends on the robustness of Eq. (1), i.e., the degree to which it actually expresses the true relationship between the measured fields at the base and reference sites. Also, to be effective as a MAD technique, the values of A , B , and C must be time-invariant; by scanning the list of decorrelating factors previously given, we see that time invariance requires that the source near-field structure must have a small effect on the coefficients (otherwise, the coefficients determined for one source configuration would possibly not work for a later, different configuration), the geological structure must be essentially invariant (probably an excellent assumption), and the sensors must be stationary.

Coefficient Evaluation

To estimate the coefficients $A(f)$, $B(f)$, and $C(f)$ in Eq. (1), we assume that the input time series $R(t)$, $X(t)$, $Y(t)$, and $Z(t)$ are digitized, and a total of N sequential discrete Fourier transforms are computed. These N FTs may be computed with some overlap in the input time series. At each discrete frequency f_o within the FT domain, we examine ψ , the squared difference:

$$\begin{aligned} \psi &= \sum_{i=1}^N \Delta_i(f) \Delta_i^*(f) \\ &= \sum_{i=1}^N \left[R_i(f) - A(f)X_i(f) - B(f)Y_i(f) - C(f)Z_i(f) \right] \\ &\quad \times \left[R_i^*(f) - A^*(f)X_i^*(f) - B^*(f)Y_i^*(f) - C^*(f)Z_i^*(f) \right]. \end{aligned} \quad (2)$$

The squared difference is clearly the logical error quantity for the determination of the coefficients. In the usual manner then we set

$$\begin{aligned}\frac{\partial \psi}{\partial \operatorname{Re}\{A(f)\}} &= \frac{\partial \psi}{\partial \operatorname{Im}\{A(f)\}} = 0, \\ \frac{\partial \psi}{\partial \operatorname{Re}\{B(f)\}} &= \frac{\partial \psi}{\partial \operatorname{Im}\{B(f)\}} = 0, \\ \frac{\partial \psi}{\partial \operatorname{Re}\{C(f)\}} &= \frac{\partial \psi}{\partial \operatorname{Im}\{C(f)\}} = 0,\end{aligned}\tag{3}$$

where $\operatorname{Re}\{\cdot\}$ and $\operatorname{Im}\{\cdot\}$ denote the real and imaginary parts, respectively. Applying the operations of Eq. (3) on the expression for Δ given in Eq. (1) yields (deleting the frequency dependence)

$$\begin{aligned}\sum_i R_i X_i^* &= A \sum_i X_i X_i^* + B \sum_i Y_i X_i^* + C \sum_i Z_i X_i^*, \\ \sum_i R_i Y_i^* &= A \sum_i X_i Y_i^* + B \sum_i Y_i Y_i^* + C \sum_i Z_i Y_i^*, \\ \sum_i R_i Z_i^* &= A \sum_i X_i Z_i^* + B \sum_i Y_i Z_i^* + C \sum_i Z_i Z_i^*.\end{aligned}\tag{4}$$

The summations involve auto- and cross-power density spectra between all combinations of the four input time series. The solution to Eq. (4) can be written in matrix form (a bar is used to denote the summation) as

$$\begin{pmatrix} A \\ B \\ C \end{pmatrix} = \begin{pmatrix} \overline{XX^*} & \overline{YX^*} & \overline{ZX^*} \\ \overline{XY^*} & \overline{YY^*} & \overline{ZY^*} \\ \overline{XZ^*} & \overline{YZ^*} & \overline{ZZ^*} \end{pmatrix}^{-1} \begin{pmatrix} \overline{RX^*} \\ \overline{RY^*} \\ \overline{RZ^*} \end{pmatrix}\tag{5}$$

at each discrete frequency in the FT domain. Equation (5) is the solution we seek for the coefficients A , B , and C in terms of quantities that can be evaluated from the four input time series. By defining

$$\underline{M} = \begin{pmatrix} \overline{XX^*} & \overline{YX^*} & \overline{ZX^*} \\ \overline{XY^*} & \overline{YY^*} & \overline{ZY^*} \\ \overline{XZ^*} & \overline{YZ^*} & \overline{ZZ^*} \end{pmatrix},$$

$$\vec{\Gamma} = (A \ B \ C)^T, \quad (6)$$

$$\vec{\rho} = (\overline{RX^*} \ \overline{RY^*} \ \overline{RZ^*})^T,$$

where the T indicates the transpose. Equation (5) can be written compactly as

$$\vec{\Gamma} = \underline{M}^{-1} \vec{\rho}. \quad (7)$$

The explicit equations for the coefficients A , B , and C can be written out from Eq. (5) using Cramer's rule [7]. The resulting expressions are very involved in the general three-dimensional case ($X, Y, Z \neq 0$). However, the essential physics of the FSB noise reduction technique can be examined by considering only the two horizontal axes at the base site. Setting $Z = 0$ in Eq. (5) and solving for A and B gives the following equations:

$$A = \frac{\sigma_R [\text{coh}(RX) - \text{coh}(RY)\text{coh}(YX)]}{\sigma_X [1 - |\text{coh}(XY)|^2]}, \quad (8)$$

and

$$B = \frac{\sigma_R [\text{coh}(RY) - \text{coh}(RX)\text{coh}(YX)]}{\sigma_Y [1 - |\text{coh}(XY)|^2]}, \quad (9)$$

where we have introduced the coherence function defined by

$$\text{coh}(ab) = \frac{\overline{ab^*}}{(\overline{aa^*} \overline{bb^*})^{1/2}}. \quad (10)$$

The identifications

$$\sigma_R = \sqrt{RR^*},$$

$$\sigma_X = \sqrt{XX^*},$$

and

$$\sigma_Y = \sqrt{YY^*}$$

for the one-sided average spectral noise densities have also been made in Eqs. (8) and (9). The coherence function, as we have defined it here, is a complex variable whose magnitude lies between 0 and 1.0 and is an indication of the phase correlation between the two signals. A value of 1.0 for $|\text{coh}(ab)|$ indicates perfect correlation, while a value of 0.0 represents no correlation.

Equations (8) and (9) reveal that problems will occur when the X and Y base site signals are highly correlated with each other, since A and B become infinite when $\text{coh}(xy) = 1$. In the data the base site cross coherences were generally found to be low, except for isolated tonal interference associated with man-made signals (such as powerline frequencies).

Alternative Derivation of the Coefficients

The above derivation of Eqs. (5), (6), and (7) for evaluating A , B , and C is exactly as given by FSB in [4]. However, by viewing the determination of the coefficients in a somewhat different manner, the equations are seen to be identical to the equations commonly used in evaluating linear system transfer functions (as given, for example, in Bendat and Piersol [8]). The demonstration of this equivalence is important, because equations for the statistical error for the transfer function are available in [8] and can be used directly to estimate errors in the determination of A , B , and C . These statistical error equations assist in the interpretation of the spectral features of the coefficients by allowing statistically significant variations to be identified.

Equation (1) can be written as

$$R - \Delta = AX + BY + CZ, \quad (11)$$

which, when Δ is forced to zero, is

$$R = AX + BY + CZ . \quad (12)$$

Hence, R appears as the output of a linear system whose inputs are X , Y , and Z , and whose transfer functions are A , B , and C respectively. Reference 8 discusses the manner in which the transfer functions of a multiple-input linear system are determined and, in particular, emphasizes the precautions that must be observed when coherent inputs are present. To demonstrate the connection between the FSB algorithm and the equations of [8], we will for simplicity set $Z = 0$ so that we consider only a two "input" system (X and Y). From [8] the equations for $A(f)$ and $B(f)$ can be written

$$A(f) = \frac{S_{RX,Y}(f)}{S_{XX,Y}(f)} , \quad (13)$$

and

$$B(f) = \frac{S_{RY,X}(f)}{S_{YY,X}(f)} , \quad (14)$$

in which the $S_{IJ,K}$ are termed residual spectra and are defined by

$$S_{RI,J} = S_{RI} \left(1 - \frac{S_{XY}S_{RJ}}{S_{JJ}S_{RI}} \right) \quad (I,J = X,Y) , \quad (15)$$

and

$$S_{I,I,J} = S_{II} (1 - \gamma_{XY}^2) \quad (I,J = X,Y) , \quad (16)$$

where

$$\gamma_{XY}^2 = |\text{coh}(XY)|^2 .$$

The notation has been taken over verbatim from [8]; the S_{IJ} are the single sided auto- and cross-power spectral densities. However, note that in terms of the notation we have used in Eq. (5),

$$S_{IJ} = \sigma_I \sigma_J \text{coh}(IJ) \quad (I,J = X,Y,R) , \quad (17)$$

and

$$S_{II} = \sigma_I^2 \quad (I = X, Y). \quad (18)$$

When Eqs. (17) and (18) are substituted into Eqs. (13) and (14) and rearranged, Eqs. (8) and (9) (the FSB equations) result. Hence, the equivalence between the FSB method and the evaluation of linear system transfer functions has been demonstrated. This equivalence will be exploited below.

Expected Noise Level of the Difference Signal Δ

The expected (theoretical) noise level of the processed difference signal Δ is of interest both for demonstration of the noise reduction capabilities of the FSB algorithm and for comparison with the experimental results. In Appendix A an expression is derived for the noise power in the processed difference signal, denoted by σ_Δ^2 , for the two-dimensional case. This equation is given by Eq. (A-4), which we repeat here:

$$\sigma_\Delta^2 = \sigma_R^2 \left[\frac{1 - \gamma_{RX}^2 - \gamma_{RY}^2 - \gamma_{XY}^2 - 2\text{Re}\{\gamma_{RX}\gamma_{RY}\gamma_{XY}\}}{1 - \gamma_{XY}^2} \right], \quad (19)$$

where

$$\gamma_{IJ}^2 = [\text{coh}(IJ)]^2 \quad (I = R, X; J = X, Y).$$

Equation (19) indicates the power in the processed difference signal is equal to the power in the reference site sensor signal modified by the factor in brackets. Three special cases can be examined that show the features of Eq. (19).

1. $\gamma_{XY} \rightarrow 1.0$. In this case σ_Δ^2 grows without limit, again emphasizing the instability in the processing when highly coherent signals are present in both base site axes. More typically $\gamma_{XY} \rightarrow 0$.

2. $\gamma_{RX} \simeq 1, \gamma_{RY} \simeq 0, \gamma_{XY} = 0$. This case corresponds to a remote sensor that is parallel to the base site X-axis in the presence of small decorrelating effects. Then Eq. (19) becomes

$$\sigma_\Delta^2 = \sigma_R^2 (1 - \gamma_{RX}^2). \quad (20)$$

Thus, the higher is the R and X coherence, the lower is the noise in the difference signal.

3. $\gamma_{RX} = \gamma_{RY} = 0$, $\gamma_{XY} = \text{any value}$. This case corresponds to an attempt to use completely uncorrelated signals at the base and reference sites to reduce the power in Δ . As expected, $\sigma_{\Delta}^2 = \sigma_R^2$ in this case, i.e. no noise reduction occurs.

Appendix A carries Eq. (19) further in order to obtain an expression for σ_{Δ}^2 in terms of both the SQUID sensor noise level (which one intuitively expects to be the ultimate limit for σ_{Δ}^2) and contributions to the noise that might not be cancelled by the construction of the algorithm (arising, for example, from nonlinear effects and possible uncorrelated noise sources other than the intrinsic sensor noise). The simple resulting equation is given by

$$\sigma_{\Delta}^2 = 2\sigma_N^2 + \epsilon\sigma_R^2, \quad (21)$$

where σ_N^2 is the SQUID sensor noise level, ϵ is a measure of the fractional deviation of the system transfer function from a linear response. The quantity ϵ is defined with greater care in Appendix A. Equation (21) indicates that the power in the difference signal is within a factor of two of the SQUID sensor noise level (for $\epsilon = 0$).

DATA COLLECTION

The data discussed in this report were collected in two widely separated geographic areas. Data sample periods of approximately two weeks duration were obtained during January 1978 at the Naval Weapons Center at China Lake, California (Lat. 36°N, Long. 118°W) and during June 1978 at Tromsø, Norway (Lat. 68°N, Long. 19°E). The China Lake location (Fig. 2) consists of flat and sandy desert terrain while the Norway location (Fig. 3) is a mountainous fjord region within the auroral zone. The base and remote site separation distances used at each area were:

- California—0.5, 4.8 and 14.6 km
- Norway—0.5, 3.5 and 9.3 km

The receiving systems employed at each site were nearly identical. The magnetometers used superconducting quantum interference devices (SQUIDs) to achieve a low intrinsic noise level and wide dynamic range. The SQUIDs were cooled by liquid helium. Table 1 lists the specifications of the four systems used in these measurements and indicates the site at which each was used. The principles of operation of a SQUID will not be discussed in this report, but the reader who is interested in more details is directed to [9].

The triaxial SQUIDs were sensitive to three orthogonal directions—two horizontal axes and a vertical axis. The SQUIDs were installed with the two horizontal directions along magnetic north-south and east-west axes. A compass and spirit level were used to perform the azimuthal alignment and establish the vertical axis. The SQUID magnetometers were buried in the soil as deeply as possible to anchor them firmly and to reduce their wind cross section. A low wooden shelter was used to shield the magnetometers from wind and the weather. Figure 4 is a photograph of the installation in California.

DINGER AND GOLDSTEIN

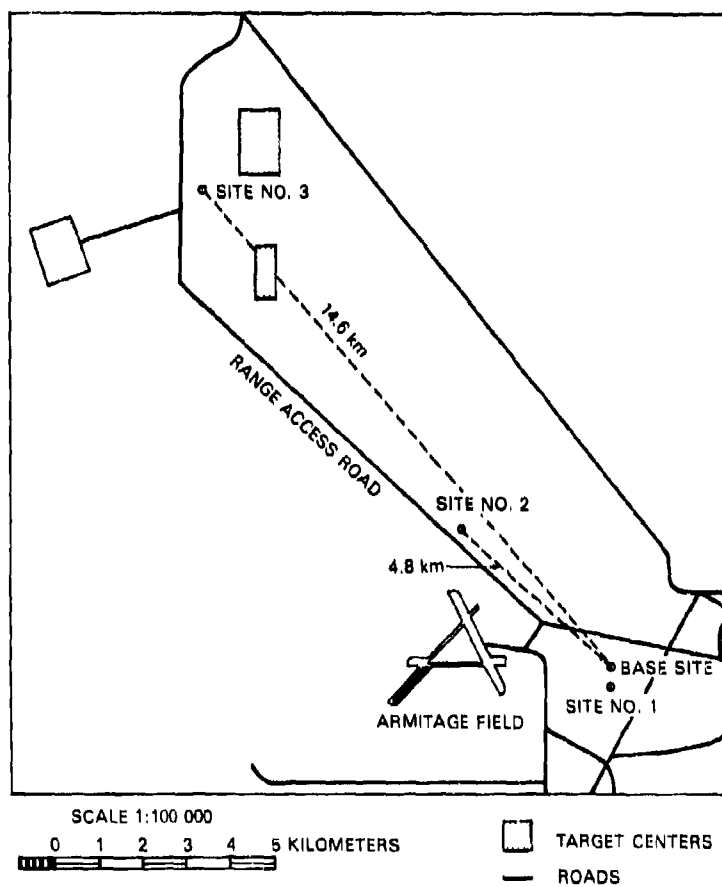


Fig. 2 -- Location of recording sites at China Lake, California

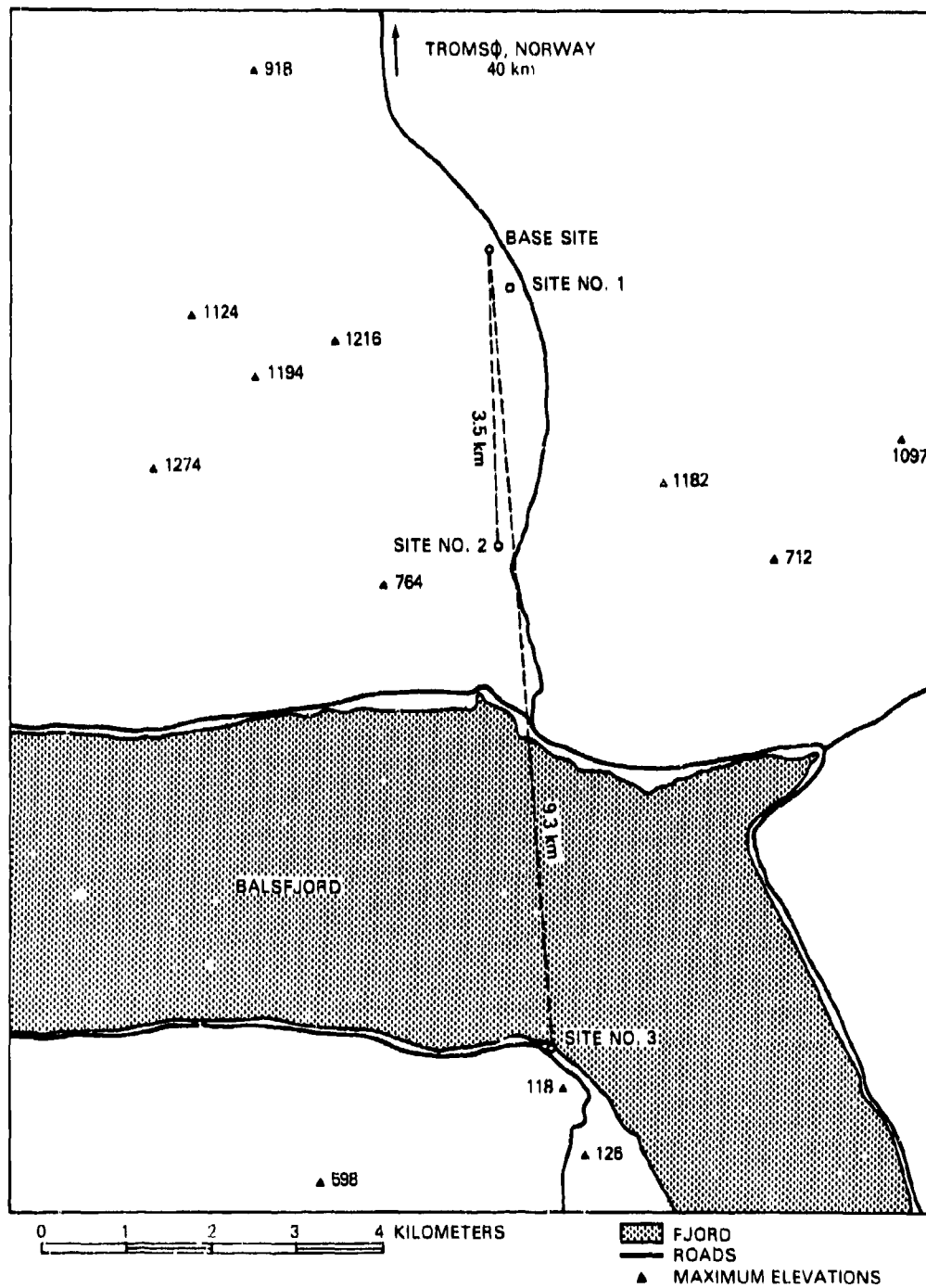


Fig. 3 — Location of recording sites near Tromsø, Norway

DINGER AND GOLDSTEIN

Table 1 — SQUID Magnetometer Systems

System (All Dynamic Ranges ≥ 130 dB)	Site	Approximate Intrinsic Noise, $\text{nG}/\sqrt{\text{Hz}}$	Internal RFI Shielding**	Liquid helium fill Interval, days
NRL-owned ELF system [10]	Calif. base	0.10	Two layers, $f_o = 86$ Hz	7
SHE Corp leased system I	Calif. remote	0.24	Single layer, $f_o = 35$ Hz	7
SHE Corp leased system II	Norway, base	<0.4	Single layer, $f_o = 37$ Hz	7
System borrowed from NCSC*	Norway, remote	0.20	None	5

*NCSC = Naval Coastal Systems Center, Panama City, Fla.

** f_o = 3dB corner frequency for RFI shields.



Fig. 4 — Typical installation of SQUID magnetometer. A wind screen is placed over the top of the magnetometer during the recording periods.

In both Norway and California it was our intention to align the axes at the separated sites in approximately the same directions, so that in the analysis R would be essentially parallel to X or Y at the base site (depending on which axis at the remote site is chosen). It is not essential for the coherence enhancement technique that R be parallel to one of the base site axes, since the coefficients in Eq. (5) in effect perform a coordinate rotation. However, for comparison with a direct difference (denoted the first difference) and for direct computation of the coherence between physically parallel axes for the two separated sites, we attempted to align the two sets of sensors as parallel as possible. (At the 0.5 km separation in Norway, however, the axes were inadvertently misaligned by an angle of about 30° .)

The signal conditioning and data recording systems are shown in Fig. 5. The SQUID field measurement noise level was preserved, and the signal to noise ratio (SNR) established, by the low noise Princeton Applied Research Model 113 preamplifier; this SNR was not degraded by the remainder of the signal path. Following the preamplifier were power frequency notch filters that used modules manufactured by Burr Brown, Model ATF76 series circuits, with $Q = 10$. The configuration consisted of three cascaded filters, with one at the primary power frequency (50 or 60 Hz) and the other two staggered by 1 Hz above and below the primary power frequency. In addition, a single filter was used at both the first and second frequency harmonics. The amplified and filtered signals at the remote site

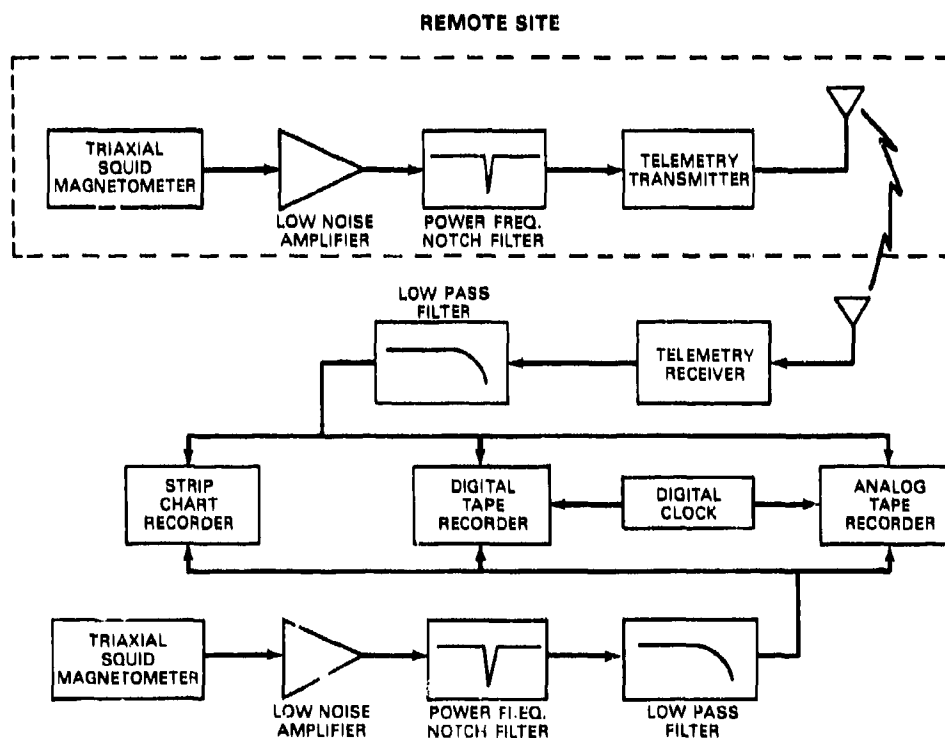


Fig. 5 — Signal conditioning and recording electronics

DINGER AND GOLDSTEIN

were input directly to an analog FM UHF telemetry system operating at a carrier frequency of 229.9 MHz. The telemetered remote site signals and the base site signals were then low pass filtered by a filter with a two pole Butterworth response with a 40-Hz corner frequency, for anti-aliasing purposes, before being recorded.

Three types of data recording were used. A hard copy was made using a pressure ink strip chart recorder, and magnetic tape recordings were produced using both an analog 14-track instrumentation tape recorder and a 12-bit digital tape recorder.

DATA ANALYSIS TECHNIQUES

The recorded data tapes were scanned, and intervals that appeared to be free of any unusual man-made interference were selected for analysis. The digital data tapes recorded in California were used directly; however, since no digital recorder was available in Norway, the analog tapes recorded there were digitized in the laboratory using a 12 bit analog-to-digital converter. The digitizing rate in both California and Norway was 83.3 Hz for each magnetometer axis, corresponding to a time sample interval of 12 ms. The periods selected for analysis are listed in Table 2.

Table 2 — Data Intervals Analyzed in this Report

Location	Separation (km)	Analysis Interval (Day/h/min)	Analysis Results in Figures	Remarks
China Lake, California	0.5	12/21/40 -12/21/50	6, 12, 17, 18	
	4.8	15/8/0 -15/8/10	7	
	14.6	18/23/20 -18/23/30	9, 13, 19	Calm conditions
		20/13/40 -20/13/50	8, 14, 20	High winds
Tromsø, Norway	0.5	173/12/20 -173/12/30	10, 15, 22	
	9.3	176/19/30 -176/19/40	11, 16, 23	

Spectral Analysis

We used a standard discrete Fast Fourier transform (FFT) program to generate sequential 1024 real point spectra for each of the magnetometer time series. Each spectrum required a total of $(1024) (.012) = 12.29$ s of data. We employed a Hanning window on each 12.29-s time slice, which we chose for its compromise between spectral resolution and leakage. The successive time slices were overlapped by 50%, so that half of the data in each time slice was "new" and half was "old". This 50% overlap is common in time series analysis and has been shown [11] to reduce the error in spectral estimation. The spectra were computed over a bandwidth of 0 to 40 Hz; this upper frequency is just below the Nyquist frequency of $(83.33/2)$ or 41.7 Hz.

Although the frequency response of the SQUID sensor is flat to at least 1 kHz, the eddy current electromagnetic interference (EMI) shields and the low pass filter introduced an amplitude and phase distortion that had to be compensated. The frequency response of each SQUID magnetometer was measured using an external drive coil to generate a known magnetic field at the sensors. This measured response was then convolved with the recorded data in order to compensate for the shield and filter high frequency roll-off.

Confidence limits for the spectra were derived in the following manner. The effective spectral bandwidth B_e is given by $B_e = (83.3 \text{ Hz}/1024)(\pi/2) = 0.128 \text{ Hz}$, where the $\pi/2$ factor is necessary to obtain the effective noise bandwidth [8]. According to Nuttall [11], the equivalent degrees of freedom N_e for 50% overlapped spectra for a total record length of T s and a Hanning window is given by

$$N_e = 2.71B_e T - 3.36. \quad (22)$$

Given a value of N_e , the 80% confidence interval spread η is given in dB by [8]

$$\eta = \frac{16}{\sqrt{N_e - 1}} \text{ dB}. \quad (23)$$

Combining Equations (22) and (23) yields

$$\eta = \frac{16}{\sqrt{2.71B_e T - 4.36}} \quad (24)$$

or, for $B_e = 0.128$ Hz,

$$\eta = \frac{16}{\sqrt{0.347T - 4.36}} \quad (25)$$

For the $T = 593$ s of data used in most of the spectra shown below, the value of $N_e = 201$, and the 80% confidence spread is 1.13 dB.

Coherence Analysis

The coherence between the nominally parallel axes at the base and remote sites was calculated from the equation

$$\gamma_{SR}^2 = \frac{|\overline{S(f)R^*(f)}|}{[\overline{S(f)S^*(f)}]^{1/2} [\overline{R(f)R^*(f)}]^{1/2}}, \quad (26)$$

where $S(f)$ and $R(f)$ are the FTs of the nominally parallel axes at the base and remote sites, respectively. The coherence is a time averaged quantity and is a measure of the time stability of the relative phase between $S(f)$ and $R(f)$. The cross-coherence between the base site X and Y sensors was also calculated using an equation similar to Eq. (26). The average for the coherence functions presented later was carried out over 593 s of data.

Confidence limits for the coherence can be derived according to the equations given in [8]. For an estimated value of coherence $\hat{\gamma}^2$ and N_e equivalent degrees of freedom, the true value of coherence γ^2 falls in the $100(1 - \alpha)$ percent confidence interval defined by

$$\tanh^2 \left[\xi - \left(\frac{1}{N_e - 2} \right) - \frac{Z_o}{\sqrt{N_e - 2}} \right] < \gamma^2 \quad (27)$$

$$< \tanh^2 \left[\xi - \left(\frac{1}{N_e - 2} \right) + \frac{Z_o}{\sqrt{N_e - 2}} \right],$$

where Z_o is the 50α percentage point of a Gaussian distribution, and

$$\xi = \frac{1}{2} \ln \frac{1 + \hat{\gamma}}{1 - \hat{\gamma}}. \quad (28)$$

The same equation for N_e can be used here as was used in deriving the spectral confidence limits, since the coherence plots below were also obtained from 50% overlapped and windowed spectra. Table 3 lists the 80% confidence limits for the coherence derived for $B_e = 0.128$ Hz, $T = 593$ s, and $N_e = 201$. The confidence interval decreases as the coherence increases.

Table 3 — Coherence 80% Confidence Limits

Estimated coherence $\hat{\gamma}^2$	0.2	0.4	0.6	0.8	0.9
Lower limit	0.13	0.33	0.54	0.76	0.88
Upper limit	0.26	0.46	0.65	0.83	0.91

FSB Analysis

The FSB algorithm was evaluated using the 50% overlapped spectra as the input data. Equation (5) was implemented on the Naval Research Laboratory Advanced Scientific Computer (ASC) in a straightforward manner to evaluate the frequency dependent parameters A , B , and C for each of the data intervals given in Table 2.

Reference 8 discusses both the bias (systematic) error and the variability (random) error associated with measuring system transfer functions. Since we have shown that evaluation of the coefficients in the FSB algorithm is equivalent to measuring a system transfer function (where R is the output and X , Y , and Z are the inputs), we can use without modification the equations given in [8]. The error equations for inputs assumed to be uncorrelated are relatively straightforward, whereas the existence of correlation between the inputs requires complicated expressions. We will use equations that assume the inputs are uncorrelated, although it will be seen below that there is a small degree of correlation between them. The correlation between inputs is sufficiently low that the uncorrelated-input expressions provide a reasonable estimate.

The bias error for A is given by

$$|\hat{A}(f)| = |A(f)| \left(1 + \frac{\sigma_{Xn}^2}{\sigma_X^2} \right)^{-1}, \quad (29)$$

where $\hat{A}(f)$ is the coefficient estimate and σ_{Xn}^2 is the extraneous noise power portion of the auto-power spectrum XX^* . Similar expressions hold for $\hat{B}(f)$ and $\hat{C}(f)$. For the data in this report the extraneous noise power results from the intrinsic sensor noise of the magnetometer; as will be shown below, the ratio σ_{Xn}^2/σ_X^2 is typically 0.01, implying that the bias error is negligible.

The variability error is expressed as a $1 - \alpha$ confidence interval for the true coefficient amplitude $|A|$ and is given by the following expression (in which the frequency dependence is suppressed):

$$|\hat{A}| - \Omega < |A| < |\hat{A}| + \Omega, \quad (30)$$

where

$$\Omega^2 = \frac{2}{N_e - 2} \left(\frac{\sigma_R^2}{\sigma_X^2} \right) (1 - \gamma_{XR}^2) F[2, N_e - 2; \alpha],$$

and $F[2, N_e - 2; \alpha] = 100 \alpha$ percentage point of an F distribution with 2 and $N_e - 2$ degrees of freedom.

The other variables in these equations have the same interpretation as given earlier. Similar equations hold for the B and C coefficient variability errors.

The confidence interval is indicated on each plot of A , B , or C in the next section. As an example of a confidence interval computation consider a typical case for X nominally parallel to R : $\gamma_{XR}^2 \approx 0.9$, $(\sigma_R^2 / \sigma_X^2) = 1.0$, $N_e = 200$, and $\alpha = 0.05$. Since $F[2, 198; 0.05] = 3.04$, the confidence interval is 0.055 for $|A|$. For this same example typically $\gamma_R^2 \approx 0.8$ and $\sigma_R^2 / \sigma_Z^2 = 1.0$; the confidence interval for $|B|$ is then 0.14. For $|C|$ typically $\gamma_Z^2 \approx 0.8$ and $\sigma_R^2 / \sigma_Z^2 = (8)^2$ (see, for example, Fig. 6 and compare R_X and Z). The confidence interval in this case for $|C|$ is 0.56, substantially larger than for A and B . Note that the confidence interval can vary with frequency, since both γ^2 and the ratio of the spectral densities depend on frequency.

RESULTS

Spectral Analysis Results

The amplitude spectra for the measured data are shown in Figs. 6 to 11. These spectra are typical for each geographic area and for each site separation distance. The spectra with labels X and Y refer to the two horizontal orthogonal axes of the triaxial SQUID magnetometers and the Z label refers to the vertical axis (See Fig. 1). The Base label corresponds to the magnetometer site for which all three sensor signals were incorporated into the geology filter, i.e., X Base refers to the term $X(f)$ in Eq. (1), etc. The Remote label corresponds to the magnetometer site for which a single sensor signal was incorporated into the geology filter, i.e., either X Remote or Y Remote refers to the term $R(f)$ in Eq. (1). The Z Remote spectra are not displayed because the vertical axis of the atmospheric noise usually contained the least amount of information (relative to the horizontal axes); hence, when an equipment outage such as telemetry channel failure or tape recorder record electronics malfunction occurred, Z Remote was always the signal sacrificed.

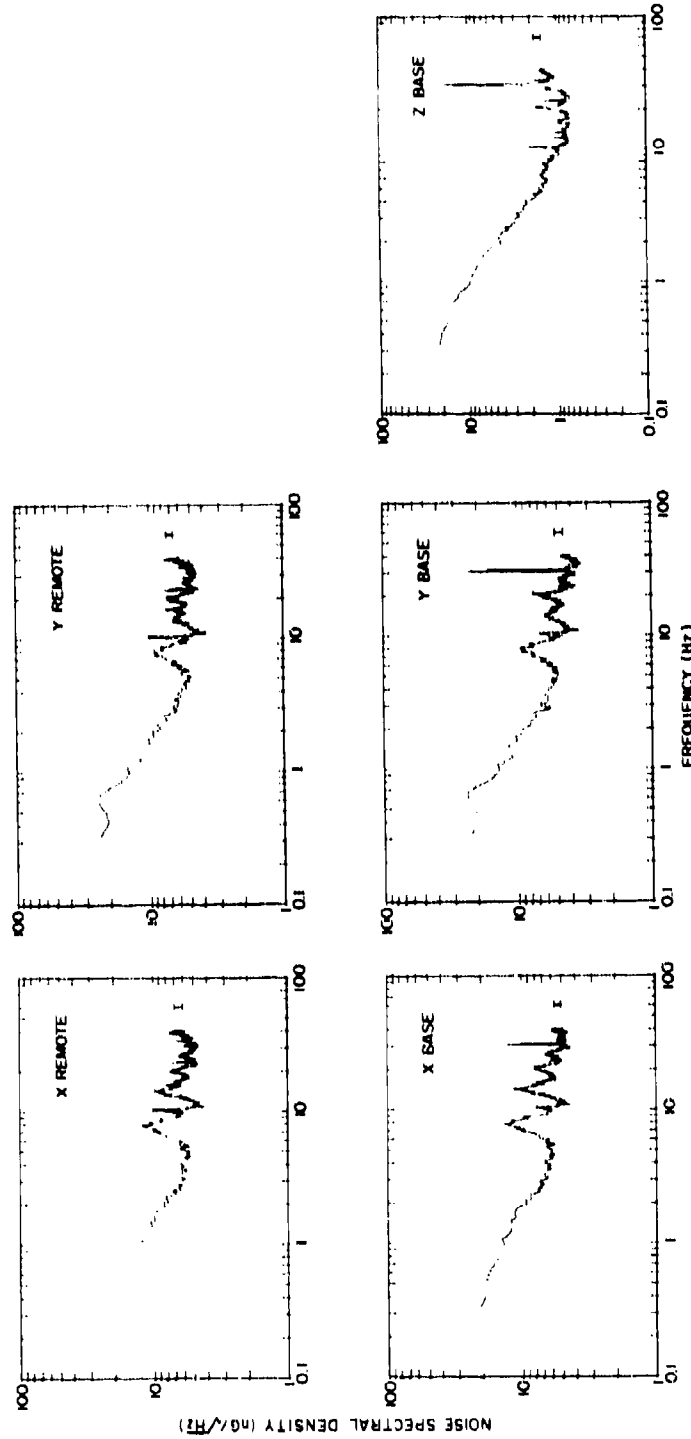


Fig. 6 — Spectra recorded in China Lake, California at 0.5 km separation. The 80% confidence interval is shown.

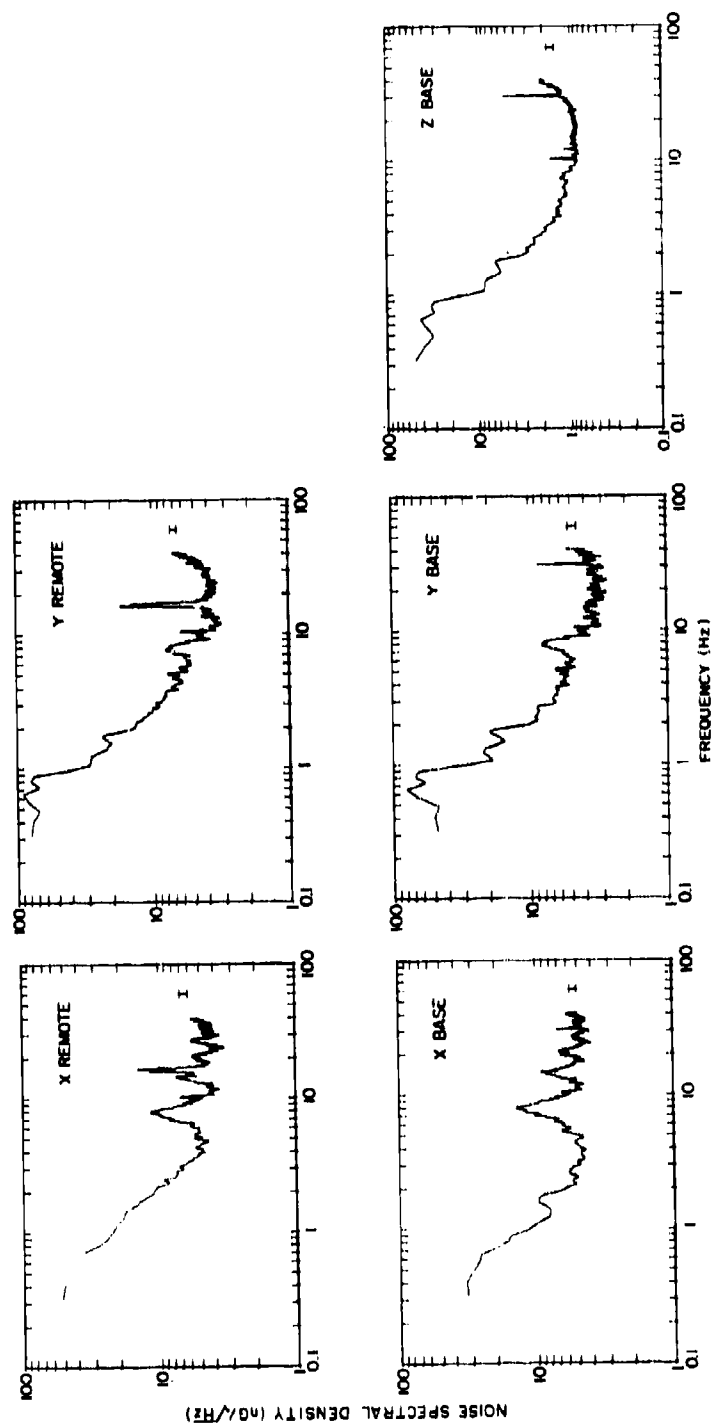


Fig. 7 — Spectra recorded in China Lake, California at 4.8 km separation. The 80% confidence interval is shown.

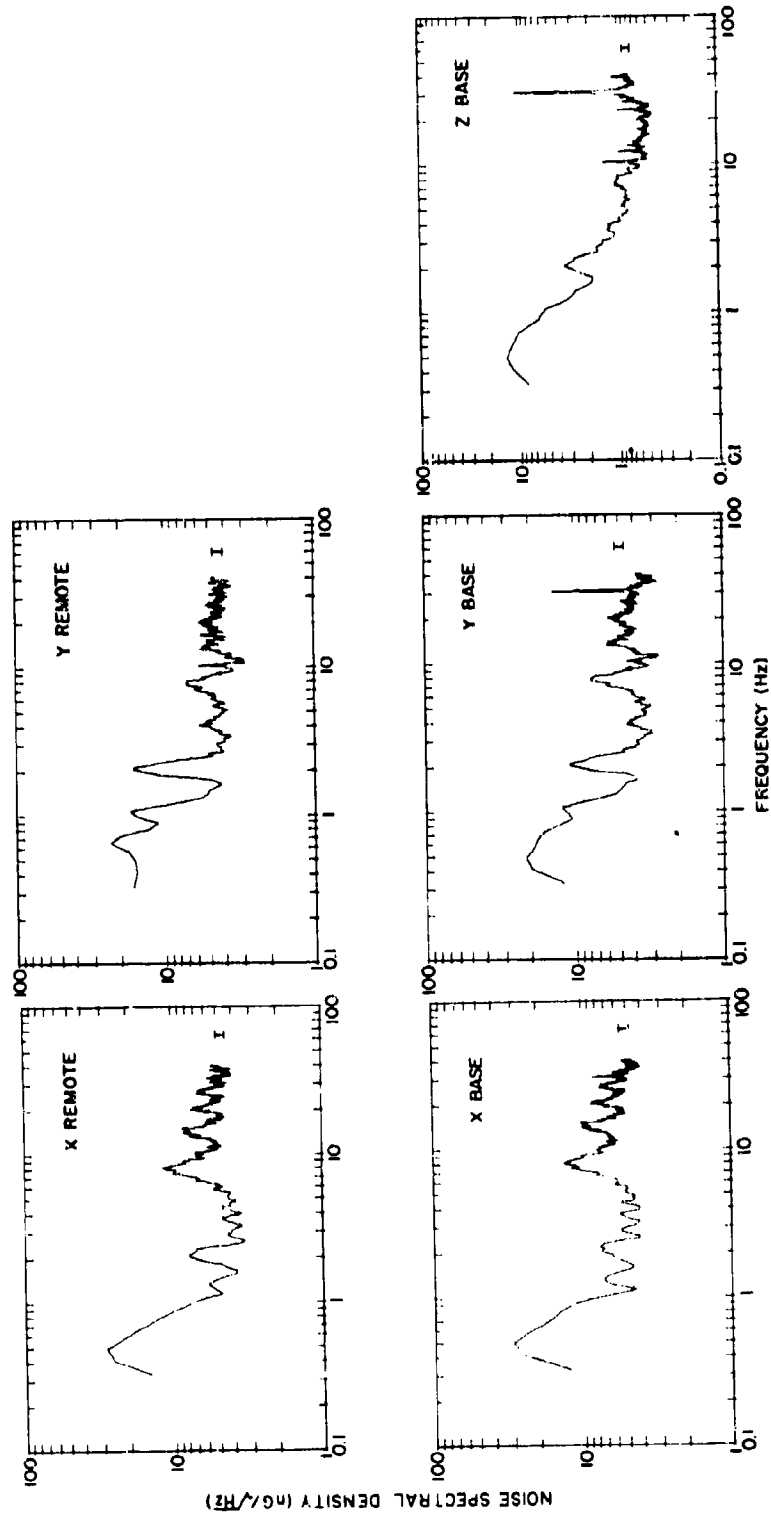


Fig. 8 — Spectra recorded in China Lake, California at 14.6 km separation, showing wind noise contamination near 2 Hz. The 80% confidence interval is shown.

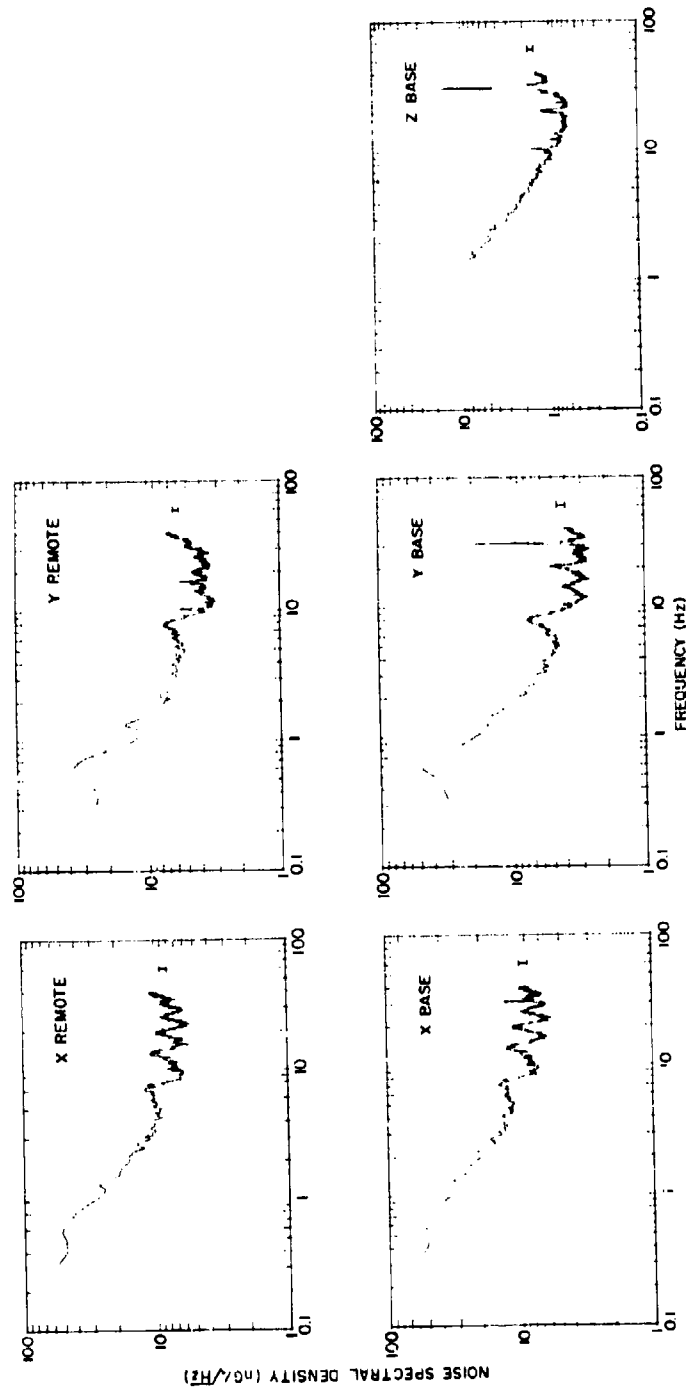


Fig. 9 — Spectra recorded in China Lake, California at 14.6 km separation during period of no wind. The 80% confidence interval is shown.

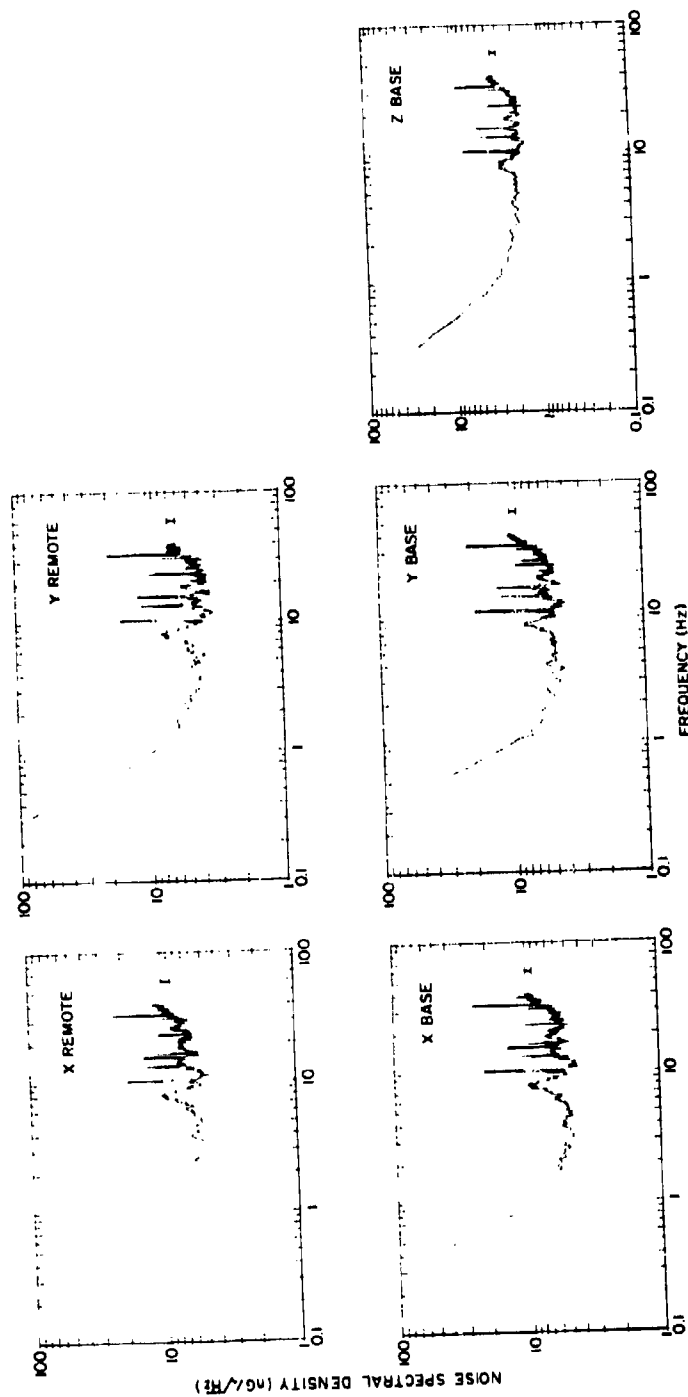


Fig 10 -- Spectra recorded near Tromsø, Norway at 0.5 km separation.
The 80% confidence interval is shown.

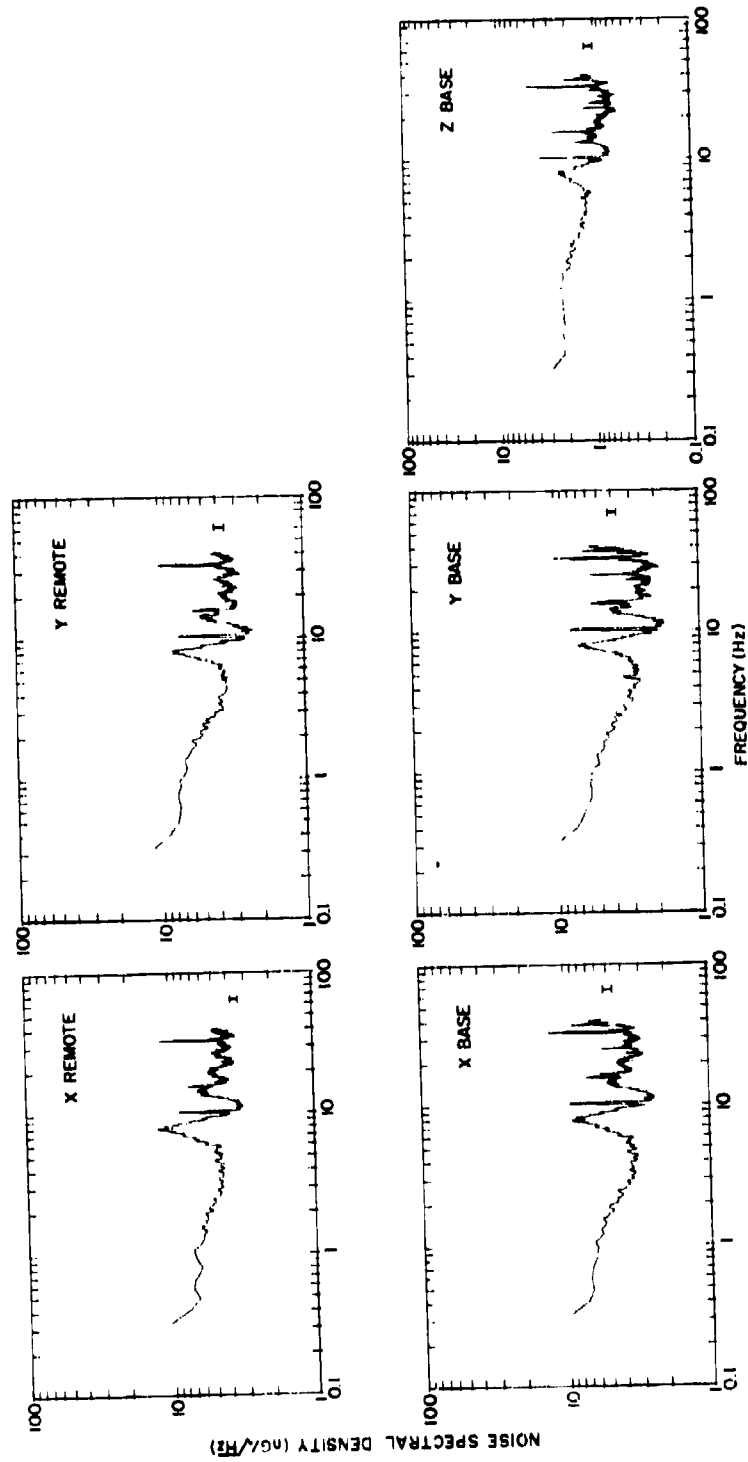


Fig. 11 — Spectra recorded near Tromsø, Norway at 9.3 km separation.
The 80% confidence interval is shown.

Each of the plots displays spectra that have been averaged for 593 s (about 10 min) of data using 50% overlap. The time given in these figures is Universal (UT); to convert to local time (LT) for the California data, $LT = UT - 8$ and for the Norway data, $LT = UT + 1$.

The most prominent features of the spectra displayed in Figs. 6 to 11 are the Schumann resonances. These resonances have a fundamental frequency in the vicinity of 7.5 to 8 Hz [12] and harmonics at frequencies of approximately 14, 20, and 26 Hz. Varying degrees of spectral features are visible at frequencies below the Schumann peaks. Figures 8 and 9 show several well defined peaks between 0.5 and 2.0 Hz that result both from micropulsation activity and micromotion of the antennas in the earth's magnetic field. In particular, the peaks near 2 Hz in Figs. 6 and 7 result from motion noise of the vector sensors in the earth's magnetic field caused by wind. Figure 9 is a second set of spectra for the 14.6 km separation in California taken during a period when there was essentially no wind. The peaks near 2.0 Hz are absent. Although the SQUID magnetometer was firmly sunk into the ground and protected by a windscreen, some motion of the magnetometer was apparently unavoidable in a strong wind.

A number of narrowband tones are evident in the spectra above about 10 Hz. The prominent tones at 10.2 Hz and (sometimes) at 20.4 Hz were caused by the tape recorder electronics. Another tone sometimes visible at 23.2 Hz has also been traced to the tape recorder electronics. The remaining tones, we feel, are caused by various types of genuine electromagnetic interference (genuine in the sense that the SQUID sensor is responding to incident signals; they are not artifacts due to subsequent processing). The tone at about 30.6 Hz, particularly evident in the California base spectra, is similar to tones frequently observed by other workers that were attributed by Lokken [13] to emissions from 4-pole, 60-Hz synchronous motors. A similar tone at 25.2 Hz in the Norway data may result from 50-Hz, 4-pole synchronous motors. Other subharmonics or near subharmonics of the local powerline frequency are sometimes visible (for example, 13.2 Hz in the Norway data) that may possibly be a result of a phenomenon described by Madden and Thompson [14]. They observed subharmonics of the local powerline frequency, which they attributed to nonlinear interactions between the generators on a power grid.

The tone at 16.7 Hz, observable in most of the Norway data, is worthy of special mention. This spike is caused either by the telephone ringing signal or by emission from Norwegian AC electrified railways. Since both frequencies are nearly the same, it is difficult to separate the two sources without further measurements.

Finally, in anticipation of the correlation analysis in the next section, the corresponding base and remote parallel axes are observed to produce spectra with very similar features; qualitatively speaking, they "look alike."

Coherence Results

Coherence plots for the data samples are presented in Figs. 12 through 16. Each of these figures shows the coherence between the two horizontal nominally parallel sensors at each site and the cross coherence between the two horizontal orthogonal sensors at the base site and at the remote site. The figures show the magnitude of γ^2 defined in Eq. (26). Confidence intervals calculated from Eq. (27) are shown for a coherence value indicated by the point within each interval.

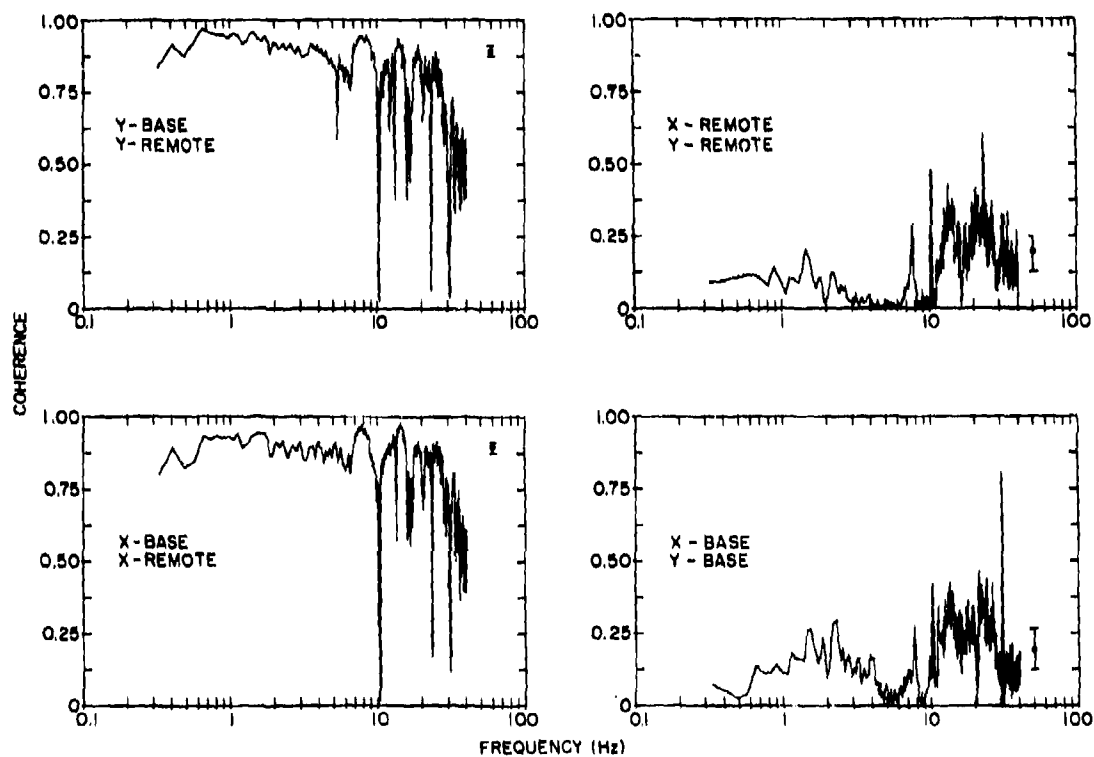


Fig. 12 — Coherence between indicated sensors for data recorded at 0.5 km separation at China Lake, California. The 80% confidence interval is shown.

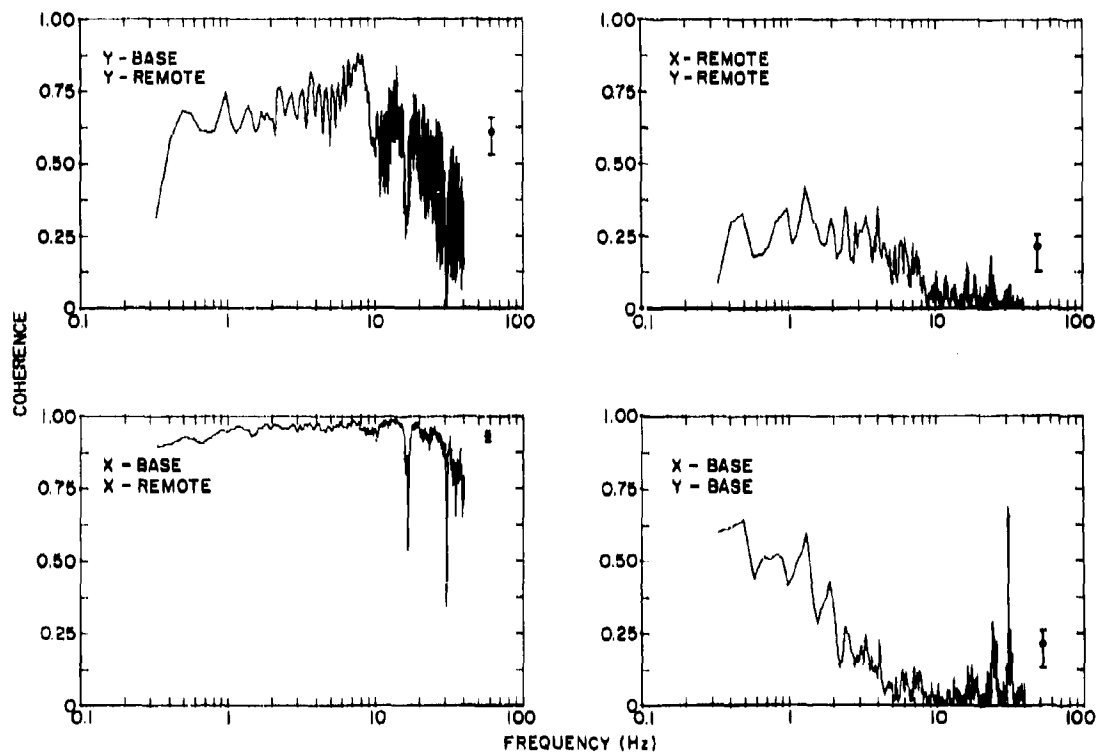


Fig. 13 — Coherence between indicated sensors for data recorded at 14.6 km separation at China Lake, California. The 80% confidence interval is shown.

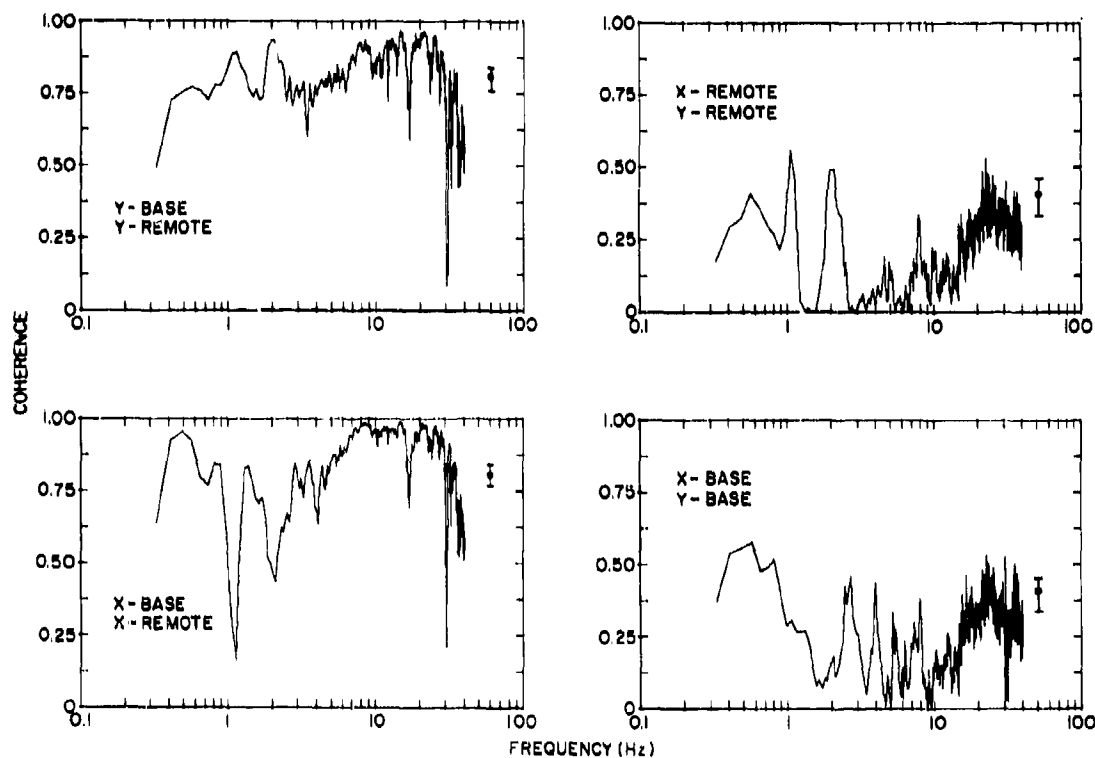


Fig. 14 — Coherence between indicated sensors for data recorded at 14.6 km separation at China Lake, California during period of high winds. The 80% confidence interval is shown.

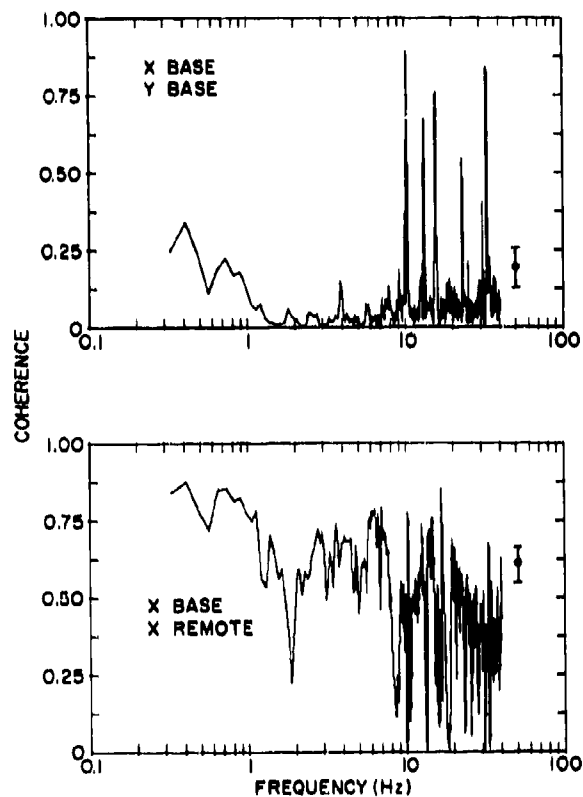


Fig. 15 — Coherence between indicated sensors for data recorded at 0.5 km separation near Tromsø, Norway. The R_y sensor was not functioning during this interval, so that the $Y-R_y$ coherence is not given. The 80% confidence interval is shown.

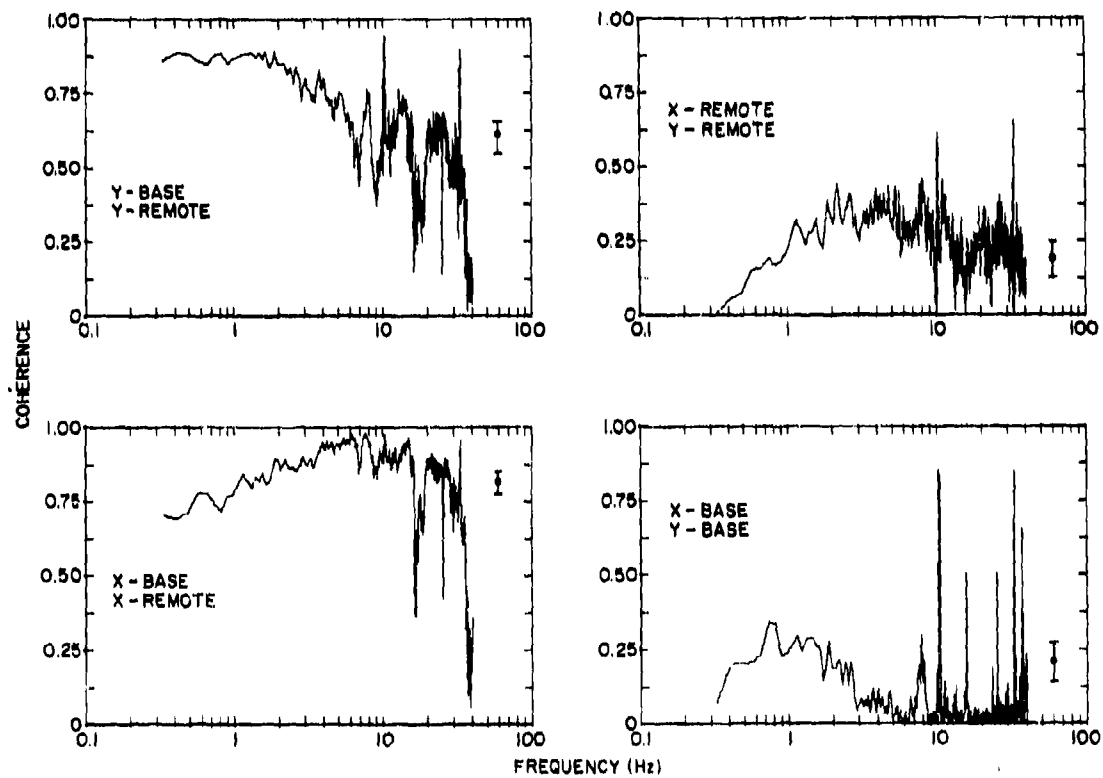


Fig. 16 — Coherence between indicated sensors for data recorded at 9.3 km separation near Tromsø, Norway. The 80% confidence interval is shown.

California Data

For a separation of 0.5 km the coherence shown in Fig. 12 below 20 Hz for both the X and Y parallel axes is relatively high (greater than 0.75). A peaking of the coherence is noticeable at the Schumann resonance frequencies, and deep nulls or peaks are evident at the frequencies of the tonal interference present in the spectra of each sensor, depending on the relative phase stability of the tones at each sensor. Above 20 Hz the coherence of the parallel sensors decreases, presumably reflecting the decrease in the coherence of the noise between the two sites at the shorter wavelengths.

At the increased separation of 14.6 km the overall coherence between the parallel sensors decreases noticeably, but not drastically. Dips again are evident at some of the frequencies of the tonal interference observed in the spectra, and the coherence decreases with increasing frequency above 20 Hz. In the coherence plot for data recorded during the high winds (Fig. 14), definite structure is visible below about 4 Hz. Especially noticeable is the dip at a frequency of 1.1 Hz in the X axis coherence. The low coherence is probably a result of the motion of the antennas in the earth's magnetic field that is uncorrelated at the two sites. In Fig. 13 the coherence between X base and X remote is about 0.9 and shows relatively little structure; however, the Y base - Y remote coherence is substantially lower. We are not certain why the east-west direction produces a lower coherence.

The coherence between the orthogonal X and Y base sensors is relatively low and variable, having an average value of about 0.25. Some of the higher variability at the lower values of coherence is due to the wider confidence intervals at low coherence (Table 3).

Norway Data

Figure 15 displays the coherence between the X axes at the 0.5 km separation in Norway. The coherence at all frequencies is substantially less than the coherence at 0.5 km measured in California, and a general decrease of the coherence with increasing frequency can be seen; a peaking of the coherence at the Schumann resonance frequencies is also evident. A somewhat lower coherence in Norway was not unexpected, since the mountainous terrain should cause more distortion of the incident noise fields. The magnitude of the decrease indicated by comparing Figs. 15 and 12, however, is much greater than we expected, particularly at the relatively close 0.5 km separation.

Before ascribing the decreased coherence in Fig. 15 to the effects of the mountainous terrain, Fig. 16 should be examined. This figure shows the coherence between the X and Y sensors for the 9.3 km separation in Norway, and for the X axes indicates that the coherence is higher than the coherence at 0.5 km. We believe that the relatively low coherence at 0.5 km in Norway (in comparison with the 9.3 km coherence) indicates an inadvertent misalignment of about 30 degrees between the two magnetometers. That is, the coherence at 0.5 km would be higher if the sensor axes were indeed parallel. This hypothesis is supported by the results of the FSB processing discussed in the next section.

The $X - R_x$ and $Y - R_y$ coherence at 9.3 km in Fig. 16 show two distinct variations. The $X - R_x$ coherence has a peak near 10 Hz, falling below this peak at higher and lower frequencies (similar to the California coherences), whereas the $Y - R_y$ coherence decreases

with increasing frequency. A possible explanation of these two variations of the coherences in terms of the local geology will be given in the next section when the FSB analysis is discussed.

As with the California data, the coherence between the base site X and Y axes is relatively low and variable.

FSB Processing Results

Figures 17 to 22 inclusive give the results of processing the recorded data according to the FSB method outlined above. Each figure contains the following plots: the coefficients A , B , and C ; the simple first difference; the processed difference; and the improvement in the difference due to the FSB processing. The first difference is the difference between the selected remote site sensor (R_x in all cases except Fig. 18) and the sensor at the base site that is nominally parallel to it (X in all cases except Fig. 18). The improvement is defined by

$$\text{Improvement} = 20 \log_{10} \frac{\text{First difference}}{\text{Processed difference}} \quad (31)$$

All plots have a logarithmic frequency scale, and the complex magnitude of the indicated quantity is plotted. All quantities were generated from 593 s of data, corresponding to approximately 200 degrees of freedom. Confidence intervals calculated from Eq. (30) are shown on the plots for A , B , and C in each case. If the interval has an appreciable variation with frequency, it is shown at spot frequencies either above or below the curve; otherwise, one interval for the entire plot is shown. The confidence interval assists in distinguishing between significant features and statistical fluctuations in the coefficient spectral variation.

California Data

Figures 17 and 18 show the results for the 0.6 km separation in California. In Fig. 17 R_x is used for the remote site axis, and in Fig. 18 R_y is used. Note that in these plots, and in other figures below, the vertical scale factor varies, depending on the maximum value plotted, so that casual visual comparison of the coefficients may be misleading.

As anticipated for this relatively short separation, in Fig. 17 the coefficient A (in this case the transfer function between the parallel sensors at the two sites) is very close to unity and displays essentially no structure or variation with frequency. The average value of A , shown by the dotted line, is 0.87. The fact that the variation of A with frequency is flat implies that the non-unity value of A is probably caused by a uniform gain difference between the X and R_x sensors, rather than by geological homogeneities (differences related to geological inhomogeneities would probably not produce a uniform effect across the frequency band). A misalignment error can be ruled out by the high coherence in Fig. 12, since an alignment error (unlike a gain difference) lowers the coherence. Coefficient B is low in amplitude, indicating that relatively little transverse component of the magnetic field at the base site has to be admixed to the difference between the nominally parallel magnetic north-oriented sensors. The spikes in both coefficient B and C are due to the various interference sources identified in the spectra of each input.

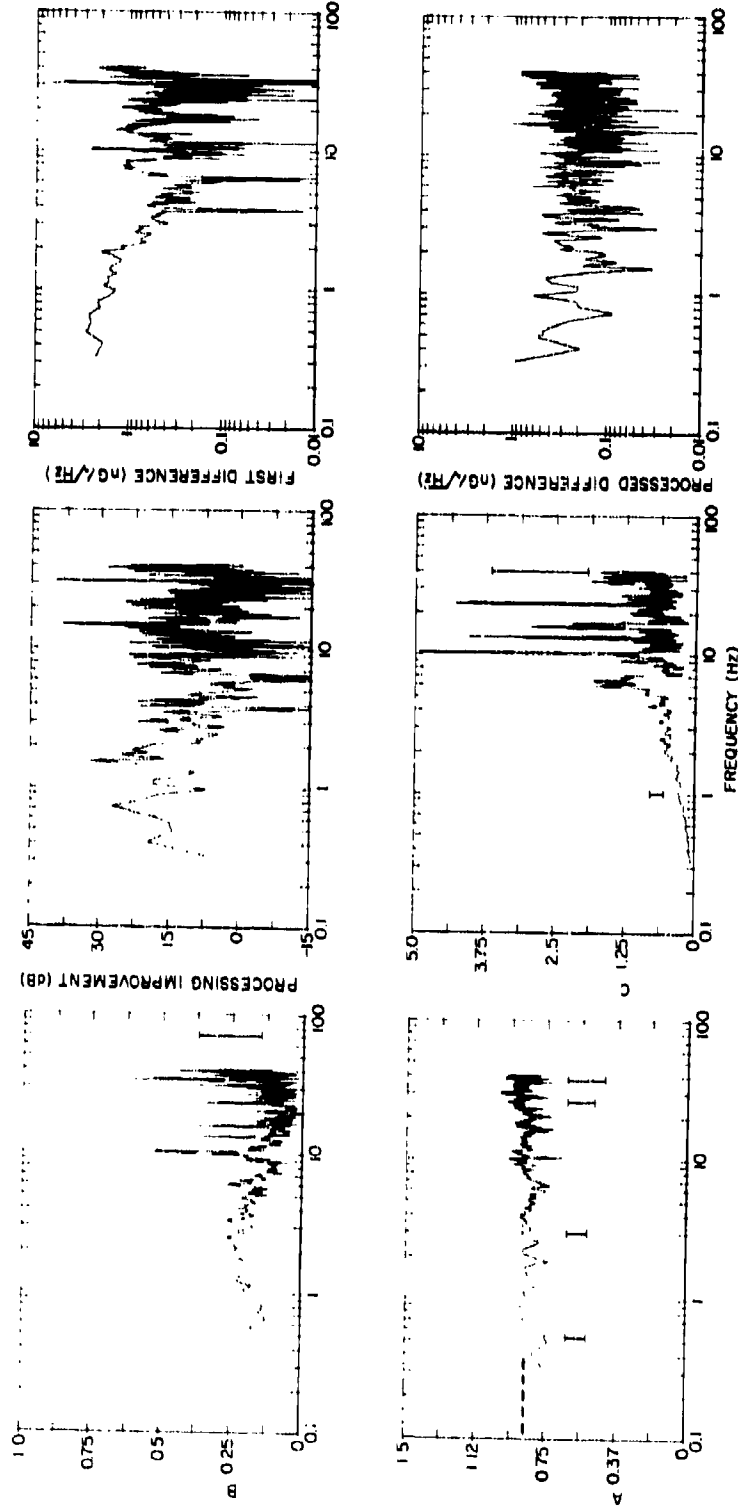


Fig. 17 — Results of FSB processing at 0.5 km separation for China Lake, California data. R_x is the remote site sensor used in the processing. The 80% confidence interval is shown.

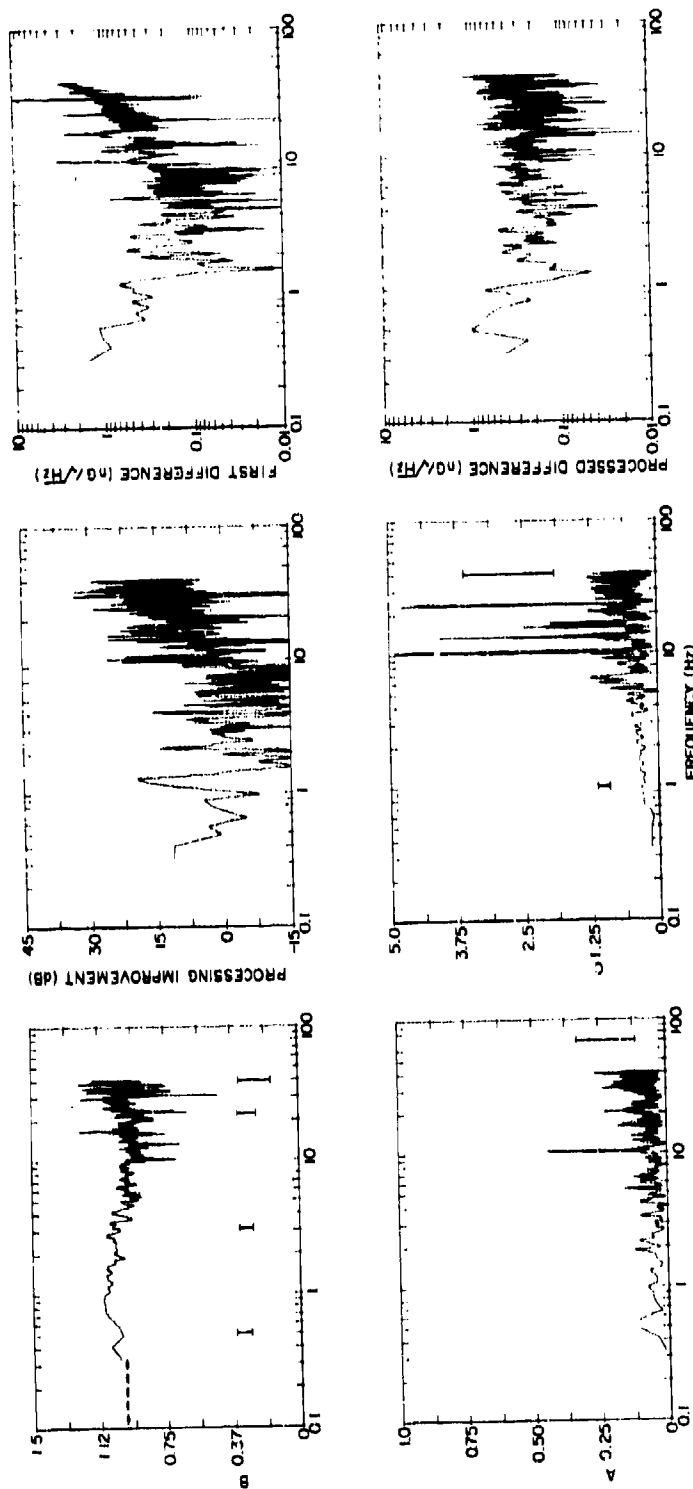


Fig. 18 — Results of FSB processing at 0.5 km separation for China, Lake, California data. R_y is the remote site sensor used in the processing. The 80% confidence interval is shown.

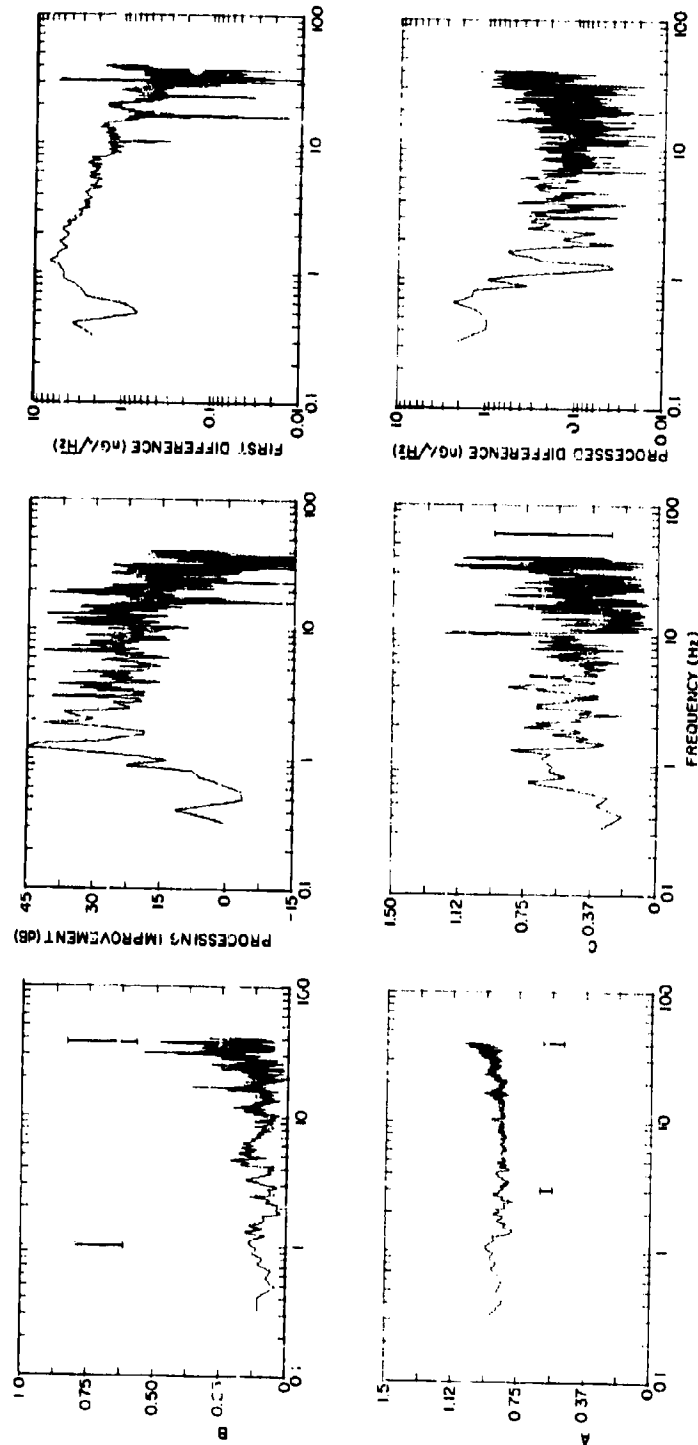


Fig. 19 -- Results of FSB processing at 14.6 km separation for China Lake, California data recorded during light winds. K_x is the remote site sensor used in the processing. The 80% confidence interval is shown.

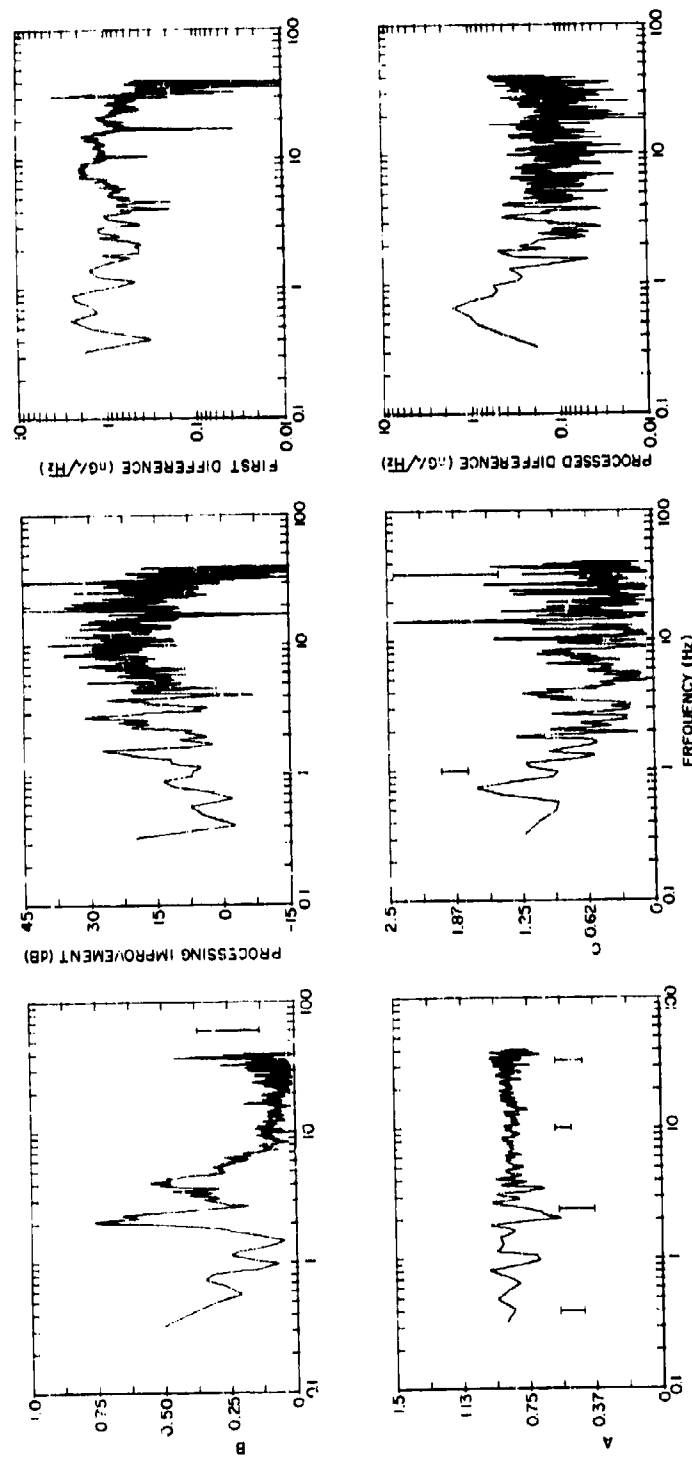


Fig. 20 — Results of FSB processing at 14.6 km separation for China Lake, California data recorded during high winds. R_x is the remote site sensor used in the processing. The 80% confidence interval is shown.

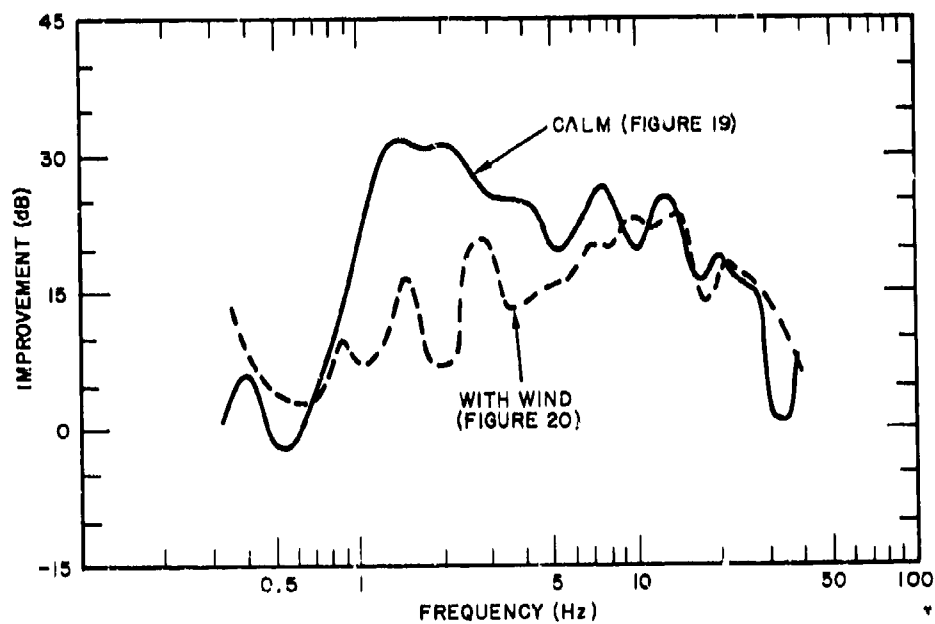


Fig. 21 — Comparison of processing improvement curves (taken from Figs. 19 and 20) for 14.6 km data recorded in China Lake, California, showing effect of wind noise contamination

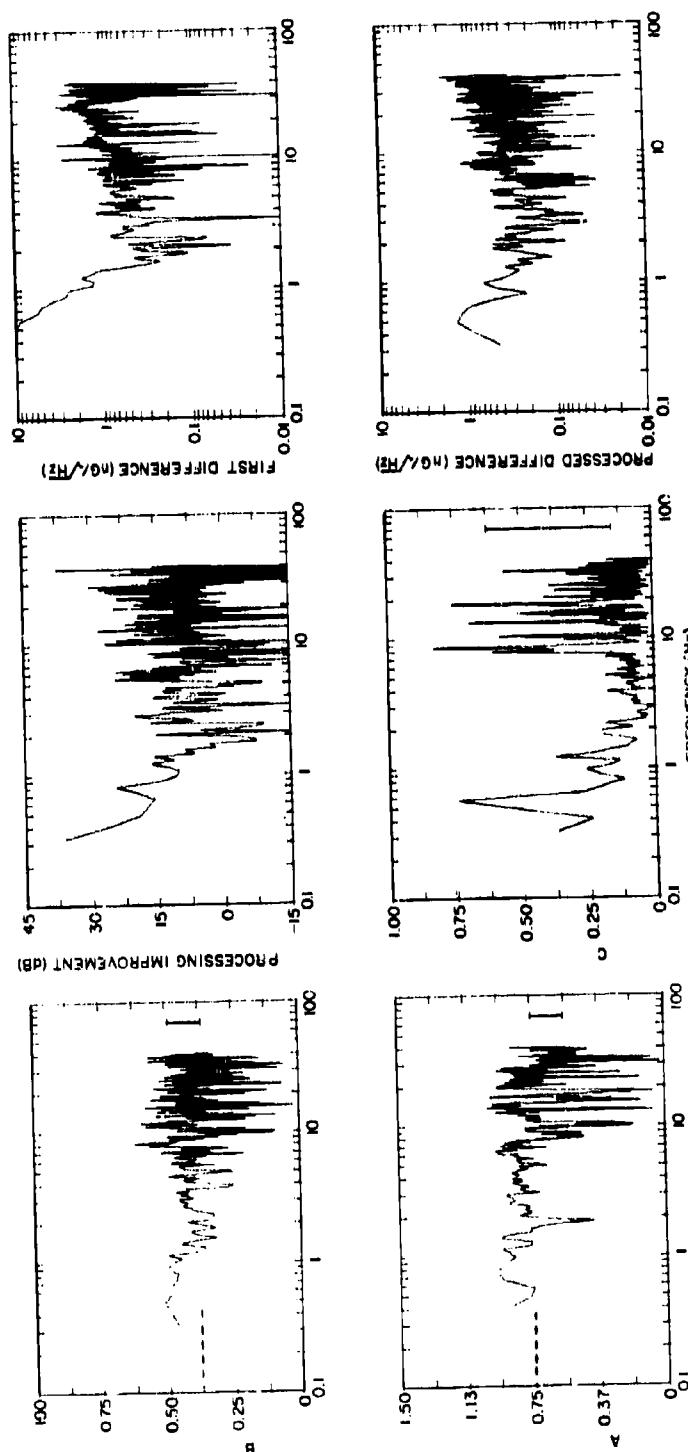


Fig. 22 — Results of FSB processing at 0.5 km separation for Tromsø, Norway data. R_x is the remote site sensor used in the processing. The 80% confidence interval is shown.

The processed difference in Fig. 17 for the 0.5 km separation is very near the average sensor noise level of 2×10^{-10} G/ $\sqrt{\text{Hz}}$ across the entire frequency band, although there is a perceptible increase in the processed difference signal at frequencies below 3 Hz. This increase, as will be seen in other cases, is present to various degrees in all of the processed differences and represents the effect of a site-to-site decorrelation factor that cannot be corrected by the FSB processing. In other words, it arises from a nonzero value of ϵ in Eq. (21). Later, we shall adduce that this increase is possibly the result of uncorrelated motion-induced signals caused by microseismic noise at the two sites. The improvement in the difference signal due to the processing is plotted in Fig. 17 and has an average value across the band of about 9 dB. A comparison with the raw spectra of this data (Fig. 8) shows that the processing suppresses ambient noise in this frequency band by up to 40 dB.

Figure 18 shows the results for the 0.5 km separation in California when R_y is taken as the single sensor at the remote site. As expected, the coefficient B is now of the order of unity and A has a low value. The average value of B shown by the dotted line is 0.98; this value implies that any gain errors in the time series data are very small for the R_y and Y axes. As in the case of the processing for R_x parallel to X at the 0.5 km separation, the processed difference level is close to the instrument noise level. The simple difference $R_y - Y$ is also close to the instrument noise level, so that the improvement due to the processing is, on the average, about 0 dB. Note that Figs. 17 and 18 are self-consistent; the gain error in R_x versus X produced a rather large difference signal that was corrected by a non-unity value of the coefficient A , so that a clear processing improvement was obtained. However, very little gain error was present between R_y and Y ; hence, the coefficient B in Fig. 18 is near unity, the simple first difference is very close to instrument noise level, and the processing yields no improvement.

Figure 19 gives results for the 14.6 km separation in California for data taken during light winds. The coefficient A is relatively flat and has a mean value of 0.86; again the evidence indicates a difference between the gains of the X and R_x sensors, rather than an alignment error. The B and C coefficients show only a small amount of structure. The large variations in coefficient C are due in part to the fact that the spectral amplitudes in the Z sensor are intrinsically lower (see Fig. 9), so that the "signal" power available to improve the site-to-site coherence is closer to the sensor noise level.

The processed difference in Fig. 19 is approximately equal to the instrument noise level between 2 and 30 Hz but exceeds the instrument noise level above and below this frequency interval. As in Fig. 17, the fact that the processed difference cannot be suppressed to near the instrument noise level (as predicted by Eq. (21)) at all frequencies may indicate the existence of a factor that cannot be corrected by the construct of Eq. (1). The improvement due to processing, also plotted in Fig. 19, is on the average about 22 dB in the 2 to 20 Hz interval. Most of this improvement is probably due to gain correction and correction for any small sensor misalignments, rather than for any geology-related corrections. This plotted improvement curve, we again emphasize, represents a comparison with the first difference. A comparison between the processed difference and the raw spectra (Fig. 9) indicates that the processing suppresses ambient noise in this frequency band by up to 40 dB.

We believe the lack of any structure or trend in the coefficients at 14.6 km indicates that any decorrelating effects due to an inhomogeneous geology are minimal at this separa-

tion. The geology at China Lake, California, is relatively homogeneous—all sites are within the large ($\sim 650 \text{ km}^2$) Indian Wells Valley, which has a uniformly layered level topology—and the sites were located at least 8.0 km from the perturbing influence of the surrounding mountains. It appears then that separations larger than 14.5 km are necessary to demonstrate the effects of a nonuniform geology at the China Lake, California site. (Data were not taken at larger separations because of the limited transmission range of the UHF telemetry link.)

Figure 20 shows the results of processing a set of data that produced definite structure in the coefficients. These data were taken at a separation of 14.5 km during a period of fairly high winds. The spectra and coherencies for this period of time were given in Fig. 8 and 14, respectively. The spectra show prominent peaks between 1 and 5 Hz that are caused by movements of the SQUID sensors in the earth's magnetic field, in spite of the use of a wind screen around the instruments. The wind motions are uncorrelated, a fact reflected in the decreased coherencies between 1 and 5 Hz in Fig. 14. The wind was gusty, so that decorrelation of the parallel sensor outputs occurs only during the gusts; hence, the plotted coherence does not decrease entirely to zero, but is depressed by an amount depending on the relative duration of the gust and quiet intervals. The X and R_x coherence is lowered more than the Y and R_y coherence. This probably occurred because the wind was blowing from the north, a circumstance that causes the magnetic north-oriented X and R_x sensors to produce a larger motion-induced signal.

The motion noise in the 1 to 5 Hz band produces the structure in the coefficients in Fig. 20. The comparison of the first difference and the processed difference in Fig. 20 shows that the processing improves the difference somewhat in the band of motion noise interference, but only to a small degree. Comparing Figs. 19 and 20, the motion noise from the wind clearly decreases the amount of improvement that the processing can achieve. To emphasize this point, in Fig. 21 smoothed processing improvement curves taken from Figs. 19 and 20 have been redrawn to show the differences. The plotted curves are the approximate average value of the improvement with variability removed. Below about 8 Hz the sample of data contaminated by wind noise shows a marked decrease in processing improvement.

This observation of the effect of motion-induced noise suggests a source of the uncorrectable decorrelating factor that causes the upturn in the processed difference curves in Figs. 17, 18 and 19 at frequencies below 2 Hz (and that causes a concomitant drop in the improvement-due-to-processing curves). A continuous background of microseismic activity is always present and is caused both by natural worldwide earthquake, tidal, and ocean wave activity and by local man-made activities (such as automobile and truck traffic) [15]. This microseismic activity has a power spectrum that increases in amplitude with decreasing frequency. It is possible that below a frequency of about 2 Hz continuous motion-induced noise caused by microseismic activity prevents the complete cancellation of noise down to the SQUID sensor noise level. We can derive an approximate value for seismic-induced magnetometer noise that serves to demonstrate at least the possibility of this noise source being observable in the processing results. Iyer and Hitchcock [16] present the results of a seismic noise survey taken in Long Valley, California, which is 200 km north of China Lake's Indian Wells Valley. The geological structure of the two valleys is similar, consisting of a soft sedimentary basin overlying a solid rock basement, so that the seismic noise values in Long

Valley should be indicative of the seismic noise background at China Lake. In the 1- to 2-Hz band the seismic background was measured [16] by a vertical velocity-sensitive seismometer to vary from 6 dB to 24 dB above a reference level of 4×10^{-8} m/s/ $\sqrt{\text{Hz}}$. The range of values reflects both a spatial and temporal variation in noise level. We shall take 18 dB (a factor of 63 in amplitude) as a reasonable median value. Assuming vertically polarized shear waves (vertical transverse motion), or SV waves, the ground motion amplitude a is related to the rate Ω by $a = \Omega/2\pi f$, where f is the frequency. Thus, at $f = 1$ Hz, there results $a = (4 \times 10^{-8})(63)/2\pi(1) = 4 \times 10^{-7}$ m/ $\sqrt{\text{Hz}}$. During the passage of an SV wave of wavelength λ , the peak tilt excursion θ_o is related to the wave amplitude A by

$$\theta_o = \frac{2\pi a}{\lambda}. \quad (32)$$

The signal ΔH induced in the X SQUID sensor (oriented magnetic north-south) when rotated through a small angle θ_o in an earth's magnetic field H_e that has a dip angle ϕ is given by [10]

$$\begin{aligned} \Delta H &= H_e \theta_o \sin \phi \\ &= \frac{2\pi a}{\lambda} H_e \sin \phi. \end{aligned} \quad (33)$$

At China Lake, $\phi = 60^\circ$ and $H_e = 0.5$ G. Values of λ were not measured in the work reported in Ref. 16, but Capon [17] quotes values of $\lambda = 4$ km as typical for seismic SV noise at 1 to 2 Hz. Substituting the values given above into Eq. (33) yields an estimate for seismic-induced noise of $\Delta H = 3 \times 10^{-10}$ G/ $\sqrt{\text{Hz}}$. This value is of the order of the level of residual noise at 1 to 2 Hz in the processed differences shown in Figs. 17, 18, and 19. The calculation indicates that seismic noise may determine the processed difference level in the lower portion of the 0.3 to 40-Hz band.

Norway Data

Figure 22 displays the results for the 0.5 km separation for the Tromsø, Norway data. These results were computed using R_x for the remote site sensor. When the SQUID instrument was installed at the 0.5-km remote site, the intention of course was to place R_x parallel to X, R_y parallel to Y, and R_z parallel to Z. However, we believe on the basis of the coherence plots in Fig. 15 and the appearance of the coefficient plots in Fig. 22 that the remote site was installed with the horizontal axes inadvertently rotated by an angle θ from the parallel alignment. In Fig. 22 a dotted line has been drawn at the average value of A and B. For axes at the remote site rotated in the horizontal plane by an angle θ , Appendix B shows that the coefficients A and B are given by

$$|A| = \frac{\cos \theta - |\gamma_{XY}| \sin \theta}{1 - \gamma_{XY}^2}, \quad (34)$$

$$|B| = \frac{\sin \theta - |\gamma_{XY}| \cos \theta}{1 - \gamma_{XY}^2}. \quad (35)$$

Appendix B emphasizes the assumptions that enter into the derivation of these equations. Given that we are interested only in an approximate value for a rotation angle, we believe that the assumptions are reasonably well satisfied. Figure 15 indicates that $\gamma_{XY}^2 \approx 0.08$ (above 5 Hz). Substituting $A = 0.75$ and $\gamma_{XY} = 0.28$ into Eq. (B-14), which is Eq. (34) solved for $\sin \theta$, gives $\theta = 32^\circ$. Similarly, substituting $B = 0.37$ and $\gamma_{XY} = 0.28$ in Eq. (B-15), which is Eq. (35) solved for $\cos \theta$, gives $\theta = 33^\circ$. These two values for the angle of rotation are in reasonable agreement, in view of the approximations used and the uncertainties in the variables. An estimate of the angle θ can also be obtained directly from the coherence plot in Fig. 15 by using Eq. (B-1):

$$[\text{coh}(R_X X)]^2 = \cos^2 \theta = 0.60, \quad (36)$$

where 0.60 is the approximate average value of the coherence between 3 and 10 Hz on Fig. 15. Equation (36) gives a value of $\theta = 39^\circ$. This value is in reasonable agreement with the values for the angle derived from the coefficient values.

Partially because the average magnitudes of the coefficients are lower, the variability across the frequency band is relatively large. Large excursions in the coefficients are also noticeable at the frequencies of the tonal interference present in the spectra (Fig. 10).

The processed difference in Fig. 22 shows a form similar to the processed differences evaluated for the California data. From 2 to 30 Hz the difference is near the SQUID sensor noise level but increases below this interval, possibly because of microseismic motion of the sensor that cannot be compensated. The simple first difference shows an unusual sharp increase below 2 Hz, presumably related to the 30° misalignment of the sensor axes. Because of this sharp increase, the improvement due to processing (relative to the first difference) in Fig. 22 is nearly 35 dB at 0.3 Hz.

Figure 23 displays the processing results for the 9.3 km separation in Norway. The coefficients contain a large amount of structure that was not observed in the other data. A large peak in all of the coefficients is noticeable at the frequency of the Schumann resonance fundamental at about 8 Hz. We have no explanation of this large peak in the coefficients except to note that the spectra for this data (Fig. 11) show an abnormally large Schumann resonance fundamental peak (relative to the resonance harmonics and the overall background level).

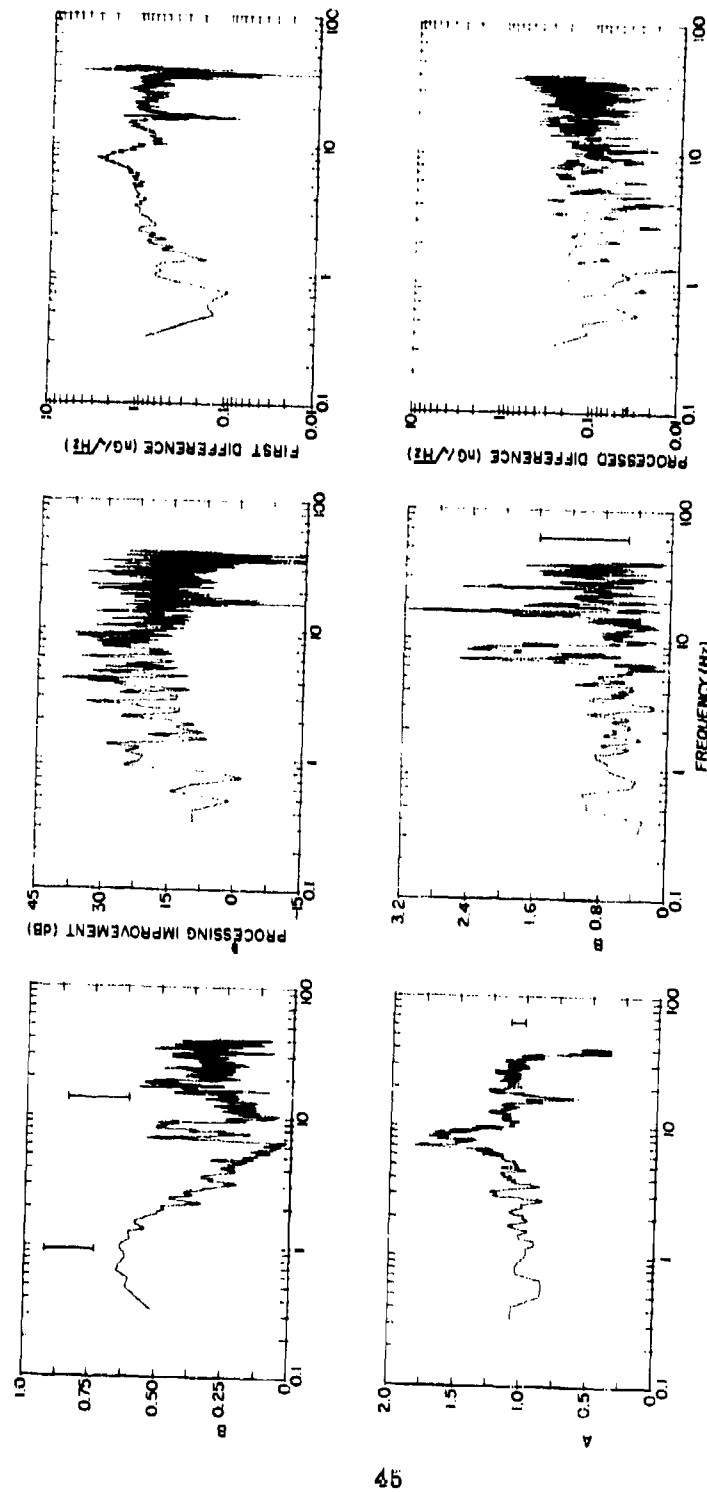


Fig. 23 — Results of FSB processing at 9.3 km separation for Tromsø, Norway data. R_x is the remote site sensor used in the processing. The 80% confidence interval is shown.

Also of interest in Fig. 23 is the large increase in B at frequencies below 6 Hz. This structure in the coefficient is probably related to inhomogeneities in the local geology. The particular feature of the geology that may cause this structure is the conductivity anomaly presented by Balsfjord, shown in Fig. 3. The form of the coefficient B indicates that as the frequency of interest is progressively decreased below 7 Hz, a larger portion of the base site Y axis (which is orthogonal to the R_x axis used in this processing) must be admixed to the difference signal formed according to Eq. (1). The conductivity anomaly presented by the fjord thus appears to rotate the incident noise fields at the remote site relative to the base site.

The processed difference in Fig. 23 falls at approximately the instrument noise level across the entire frequency interval. The increase in the difference level at frequencies below 2 Hz is not as pronounced as the increase in the processed differences given in Figs. 17 through 20, and in Fig. 22. The improvement in the difference due to the processing has a maximum value of about 20 dB at 10 Hz. Comparing the raw spectrum in Fig. 11 for the X base sensor with the processed difference indicates that ambient noise is suppressed by 35 dB by the processing.

CONCLUSIONS AND RECOMMENDATIONS

No substantial differences were observed between the California data and the Norway data in either the characteristics of the noise or the ability of the FSB algorithm to suppress the noise. In both locations the FSB algorithm was able to reduce the ambient noise essentially to the SQUID instrumental noise level. A small increase in the processed difference noise level below 5 Hz is probably a result of seismic-induced motion noise for which the FSB processing cannot compensate.

For a detection application of the FSB processing, the reduction in ambient noise achievable when the processed difference is evaluated using fresh time series data with coefficients determined many hours earlier must be investigated. We have not yet processed the data in this manner but hope to address this point in a future report.

The usefulness of component differencing as a geophysical exploration technique depends on the ease with which the specific form of the coefficients can be interpreted (with the aid of a mathematical model) in terms of subsurface geological features. The development of the theory to explain the specific form of the coefficients (and the coherence) measured at the 9.3-km separation in Norway, where geological effects due to the fjord clearly were observed, is a worthwhile area for further work.

Finally, the numerous adaptive noise suppression techniques described in the literature by Widrow [18], Griffiths [19], and others should also be applied to the data taken in this study for comparison with the FSB algorithm. We hope to make this comparison as a continuation of the present study.

ACKNOWLEDGMENTS

The field measurements described in this report required the assistance of many people in the cooperating organizations. Dr. Jim Battles at the Naval Weapons Center arranged the liquid helium logistics and the measurement sites, and he graciously permitted us to use his laboratory during our stay. We are also indebted to Dave White and Fred Essig of NWC for assistance during the China Lake measurements.

The Norwegian site was made available by the Norwegian Defence Research Establishment (NDRE). Fulfilling the need for liquid helium required near-heroic measures at times, and we are grateful to Dr. E. Thrane of NDRE both for his assistance in obtaining the sites and his arrangements for the liquid helium logistics. We are also grateful for the hospitality and assistance offered by the two Norwegian families along Balsfjord who allowed us to establish remote sites on their land.

The remote site SQUID magnetometer used in Norway was loaned to us by the Naval Coastal Systems Center in Panama City, Florida. We are grateful to Dr. Ron Clark for the loan of this instrument.

Finally, we acknowledge the numerous important contributions to these measurements of William Meyers at NRL.

REFERENCES

1. A. C. Fraser-Smith and J. L. Buxton, "Superconducting Magnetometer Measurements of Geomagnetic Activity in the 0.1- to 14-Hz Frequency Range," *J. of Geophysical Research*, 80, pp. 3141-3147, August 1975.
2. J. L. Buxton and A. C. Fraser-Smith, "A Superconducting System for High Sensitivity Measurements of Pc 1 Geomagnetic Pulsations," *IEEE Trans. Geosci. Electronics*, 12, 109-113, 1974.
3. J. E. Zimmerman and W. H. Campbell, "Tests of Cryogenic SQUID for Geomagnetic Field Measurements," *Geophysics*, 40, pp. 269-284, 1975.
4. B. C. Fowler, H. W. Smith, and F. X. Bostick, "Magnetic Anomaly Detection Utilizing Component Differencing Techniques," Technical Report 154 for Contract N00014-67-A-0126-0011, Electrical Geophysics Research Laboratory, University of Texas at Austin, August 31, 1973.
5. T. D. Gamble, W. M. Goubau, and J. Clarke, "Magnetotellurics with a Remote Magnetic Reference," *Geophysics*, 44, pp. 53-68, 1979.
6. T. D. Gamble, W. M. Goubau, and J. Clarke, "Error Analysis for Remote Reference Magnetotellurics," *Geophysics*, 44, pp. 959-968, 1979.
7. F. B. Hildebrand, *Methods of Applied Mathematics*, 2nd ed., Prentice-Hall (Englewood Cliffs, New Jersey), 1965.
8. J. S. Bendat and A. G. Piersol, *Random Data: Analysis and Measurements Procedures*, John Wiley and Sons (New York), 1971.

9. J. Clarke, "Low Frequency Applications of Superconducting Quantum Interference Devices," *Proc. of IEEE*, 61, pp. 8-19, January 1973.
10. R. J. Dinger, J. R. Davis, J. A. Goldstein, W. D. Meyers, M. Nisenoff, S. A. Wolf, and J. J. Kennedy, "SQUID ELF Receiving Antenna for Submarine Applications: Final Report," *NRL Report 8118*, 25 May 1977.
11. A. H. Nuttall, "Spectral Estimation by Means of Overlapped Fast Fourier Transform Processing of Windowed Data," *Naval Underwater Systems Center Report No. 4169*, 13 October 1971 (AD 483,829).
12. J. Galejs, "Frequency Variations of Schumann Resonances," *J. Geophysical Res.*, 75, pp. 3237-3251, 1970.
13. J. E. Lokken and J. A. Shand, "Man-Made Electromagnetic Interference at Extremely Low Frequencies," *Canadian J. of Physics*, 42, pp. 1902-1907, October 1964.
14. T. Madden and W. Thompson, "Low-Frequency Electromagnetic Oscillations of the Earth-Ionosphere Cavity," *Rev. Geophys.* 3, p. 211, 1965.
15. K. E. Bullen, *An Introduction to the Theory of Seismology*, Cambridge University Press (London), 1963.
16. H. M. Iyer and T. Hitchcock, "Seismic Noise Survey in Long Valley, California," *J. Geophysical Research*, 81, pp. 821-840, February 1976.
17. J. Capon, "Signal Processing and Frequency-Wavenumber Spectrum Analysis for a Large Aperture Seismic Array," in *Methods in Computational Physics*, 13, Academic Press (New York), 1973.
18. B. Widrow, J. R. Glover, Jr., J. M. McCool, J. Kaunitz, C. S. Williams, R. H. Hearn, J. R. Zeldler, E. Dong, and R. C. Goodlin, "Adaptive Noise Cancelling: Principals and Applications," *Proc. IEEE*, 63, pp. 1692-1716, December, 1975.
19. L. Griffiths and R. Medaugh, "Convergence Properties of an Adaptive Noise Cancelling Lattice Structure," *Proc. 1979 Conf. on Decision and Control*, San Diego, January 1979.

Appendix A

PROCESSED DIFFERENCE NOISE LEVEL

This appendix derives an expression for the noise level of the processed difference signal Δ . Explicit computation of the noise level of Δ is very complicated for the general 3-dimensional case, and hence we calculate it for a 2-dimensional case ($Z = 0$). The 2-dimensional calculation is sufficient for deriving an expression to compare with experiment.

The equation that A and B should satisfy is of course given by

$$\Delta = R - AX - BY. \quad (\text{A-1})$$

We now seek the average noise power in Δ , denoted σ_Δ^2 , when A and B (as evaluated in Eqs. (8) and (9)) are used with a series of measurements of R , X , and Y :

$$\sigma_\Delta^2 = \frac{1}{N} \sum_i \Delta_i \Delta_i^* = \frac{1}{N} \sum_i (R - AX_i - BY_i)(R_i^* - A^* X_i^* - B^* Y_i^*). \quad (\text{A-2})$$

Substituting Eqs. (8) and (9) into Eq. (A-2) and making use of the identity

$$(f + g)(f^* + g^*) = |f|^2 + |g|^2 + 2 \operatorname{Re} \{fg\}, \quad (\text{A-3})$$

the following expression results after tedious algebra:

$$\sigma_\Delta^2 = \sigma_R^2 \left(\frac{1 - \gamma_{RX}^2 - \gamma_{RY}^2 - \gamma_{XY}^2 + 2 \operatorname{Re} \{ \gamma_{RX} \gamma_{RY} \gamma_{XY} \}}{1 - \gamma_{XY}^2} \right), \quad (\text{A-4})$$

where the notation $\gamma_{IJ} = \operatorname{coh}(IJ)$ ($I = R, X; J = X, Y$) has been used. Several limiting forms of Eq. (A-4), and their implications, are examined in the text under *Expected Noise Level of the Difference Signal*.

We now develop an expression for the coherence that separates the effect of the uncorrelated intrinsic sensor noise from the portion of the signals measured at each site that are possibly coherent. This expression is to be substituted into Eq. (A-4) to obtain an estimate of σ_Δ^2 . We assume that the measured FT's can be written as:

$$\begin{aligned} X(f) &= X_c(f) + X_n(f), \\ Y(f) &= Y_c(f) + Y_n(f), \text{ and} \\ R(f) &= R_c(f) + R_n(f), \end{aligned} \quad (\text{A-5})$$

where the subscript c refers to a "true" signal that may be correlated at the base and reference sites, and the subscript n refers to uncorrelated noise components arising, for example, from the intrinsic sensor noise. If we use as an example X and R from Eq. (A-5), the coherence function γ_{XR}^2 of Eq. (26) can be written (dropping the explicit frequency dependence) as

$$\gamma_{XR}^2 = \frac{\tilde{\gamma}_{XR}^2}{1 + \frac{\sigma_{Xn}^2}{\sigma_{Xc}^2} + \frac{\sigma_{Rn}^2}{\sigma_{Rc}^2} + \left(\frac{\sigma_{Rn}^2}{\sigma_{Rc}^2} \right) \left(\frac{\sigma_{Xn}^2}{\sigma_{Xc}^2} \right)}, \quad (\text{A-6})$$

where

$$\tilde{\gamma}_{XR}^2 = \frac{|\overline{X_C R_C^*}|^2}{(\overline{X_C X_C^*}) (\overline{R_C R_C^*})} \quad (\text{A-7})$$

is the true coherence between the signals. As one would expect, the additive sensor noise causes the measured coherence to be less than the true coherence. Similar equations can be written for γ_{YR}^2 and γ_{XY}^2 . The ratios $(\sigma_{Xn}^2/\sigma_{Xc}^2)$ and $(\sigma_{Rn}^2/\sigma_{Rc}^2)$ in the denominator of Eq. (A-6) are the noise power to signal power ratios of the sensors (signal here refers to the true external signals incident on the SQUID magnetometers); as will be seen in the data discussed below, these ratios are approximately equal for all sensors and are no larger than about 0.01. Therefore, let these ratios be denoted δ . Then Eq. (A-6) can be written:

$$\gamma_{XR}^2 = \frac{\tilde{\gamma}_{XR}^2}{1 + 2\delta + \delta^2} \approx \tilde{\gamma}_{XR}^2 (1 - 2\delta), \quad (\text{A-8})$$

where the fact that $\delta \ll 1$ has been used to obtain the approximation. If Eq. (A-8) and a similar equation for γ_{YR}^2 are substituted into Eq. (A-4), the following expression results, where, for simplicity, $\gamma_{XY}^2 = 0$ has been assumed:

$$\sigma_\Delta^2 = \sigma_R^2 \left[1 - \tilde{\gamma}_{RX}^2 - \tilde{\gamma}_{RY}^2 + 2\delta (\tilde{\gamma}_{RX}^2 + \tilde{\gamma}_{RY}^2) \right]. \quad (\text{A-9})$$

Again viewing the noise cancellation process as the measurement of an input (X and Y) - output (R) linear system transfer function, [8] shows that if the system is strictly linear, then:

$$\tilde{\gamma}_{RX}^2 + \tilde{\gamma}_{RY}^2 = 1 \quad (\text{A-10})$$

always. This suggests that the existence of any nonlinear effects and uncorrelated noise sources other than the intrinsic sensor noise can be quantified by a parameter ϵ by letting:

$$\epsilon = 1 - \tilde{\gamma}_{RX}^2 - \tilde{\gamma}_{RY}^2 \quad (\text{A-11})$$

Substituting Eq. (A-11) into Eq. (A-9) gives

$$\sigma_{\Delta}^2 = \sigma_R^2 (\epsilon + 2\delta), \quad (\text{A-12})$$

where the term $2\delta\epsilon$ has been dropped on the assumption that it is a second order term. Noting that

$$\frac{\sigma_{Rn}^2}{\sigma_R^2} = \frac{\sigma_{Rn}^2}{\sigma_{RC}^2 + \sigma_{Rn}^2} = \frac{\sigma_{Kn}^2}{\sigma_{RC}^2 \left(1 + \frac{\sigma_{Rn}^2}{\sigma_{RC}^2}\right)} = \frac{\delta}{1 + \delta} \approx \delta, \quad (\text{A-13})$$

Eq. (A-12) can be written

$$\sigma_{\Delta}^2 = 2 \sigma_{Rn}^2 + \epsilon \sigma_R^2. \quad (\text{A-14})$$

Equation (A-14) is the simplest possible equation for the noise power in the difference signal and demonstrates that the FSB differencing technique decreases the noise power to approximately the noise level of the sensors (the factor of 2 arises from the fact that the sensors are used pair wise) plus a residual amount arising from nonlinearities or uncorrelated noise sources. Although γ_{XY}^2 was set equal to zero to go from Eqs. (A-4) to Eq. (A-14), a finite value of γ_{XY}^2 makes Eq. (A-14) somewhat more complicated but does not change the conclusions.

Appendix B

THE EFFECT OF AN ANGULAR MISALIGNMENT ERROR

This appendix derives an expression for the coefficients A and B when the base site horizontal axes and the remote site horizontal axes are rotated with respect to each other by an angle θ . The expressions are derived by making the following simplifying assumptions:

- Only the horizontal axes are considered, i.e., a two-dimensional case with $Z = 0$ is used.
- Only decorrelating effects from misalignment are considered, i.e., geological inhomogeneities are not explicitly included in any manner.

Equations (8) and (9) given an explicit expression for A and B in the two-dimensional case. The misalignment of the axes at the base and remote sites causes the coherence functions that appear in these equations to be reduced. We assert that the dependence of the coherence on a presumed misalignment θ between the X and R axes is given approximately by

$$|\text{coh}(XR)| = \cos \theta. \quad (\text{B-1})$$

We can demonstrate this dependence heuristically in the following manner. The cross-spectra that enter into the numerator of the coherence function defined in Eq. (10) or Eq. (26) can be represented by [8]

$$X(f)R(f) = \lim_{\Delta f \rightarrow 0} \lim_{T \rightarrow \infty} \frac{1}{(\Delta f)T} \int_0^T X(t, f, \Delta f) R^*(t, f, \Delta f) dt, \quad (\text{B-2})$$

where $X(t, f, \Delta f)$ and $R(t, f, \Delta f)$ are X and R time series that have been filtered through a (narrow) band pass filter Δf . The time series $X(t)$ and $R(t)$ for ULF and ELF noise can be represented as the superposition of many overlapping random wave packets, as shown in Fig. B-1; these packets arise from the filtering at a relatively low frequency f of atmospheric impulses whose inverse pulse width is much larger than f . Referring to Fig. B-2, we can then write the signals $R(t)$ and $X(t)$ as follows:

$$X(t) = \sum_i F(\tau_i, D_i, H_i) e^{j2\pi f t} \cos \varphi_i, \quad (\text{B-3})$$

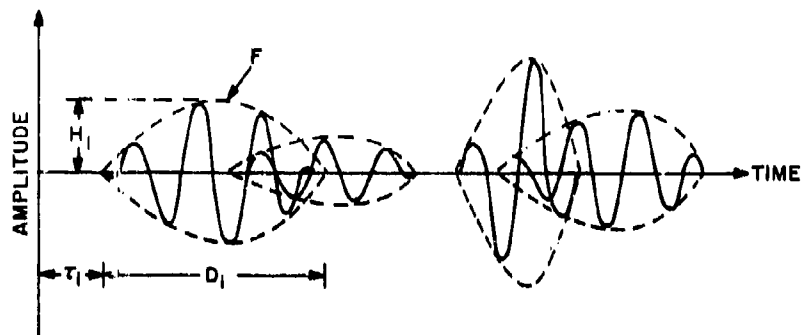


Fig. B-1 — Generalized representation of ELF wavepackets that sum together to form the recorded noise voltage

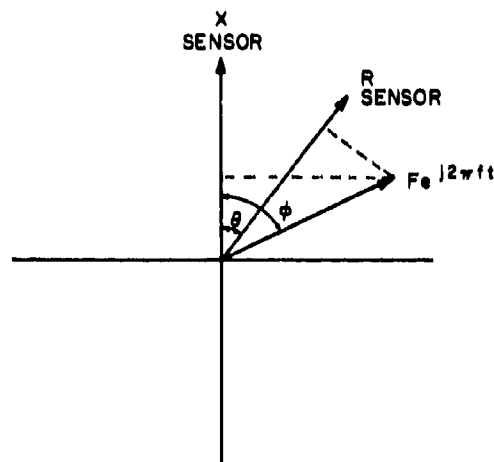


Fig. B-2 — Geometry of X and R sensors with a misalignment of θ , and plane-polarized incident wave at angle ϕ

and

$$R(t) = \sum_i F(\tau_i, D_i, H_i) e^{j2\pi ft} \cos(\phi_i - \theta), \quad (\text{B-4})$$

where $F(\tau_i, D_i, H_i)$ is a generalized representation of the individual wavepacket envelopes with start time τ_i , duration D_i , and peak amplitude H_i . As Fig. B-2 indicates, ϕ_i is the azi-

muthal arrival angle of the packet. The quantities τ_i , D_i , H_i , and φ_i are assumed to be random variables.

Forming the product needed in Eq. (B-2) gives

$$XR = \sum_i \sum_k F(\tau_i, D_i, H_i) F^*(\tau_k, D_k, H_k) \cos \varphi_i \cos(\varphi_k - \theta). \quad (\text{B-5})$$

The cross terms in the summation will, on the average, sum to zero because of the random nature of the wave packets. There remains:

$$XR = \sum_i F^2(\tau_i, D_i, H_i) \cos \varphi_i \cos(\varphi_i - \theta). \quad (\text{B-6})$$

The denominator in Eq. (26) for the coherence is found in a similar manner. The two terms are:

$$XX = \sum_i F^2(\tau_i, D_i, H_i) \cos^2 \varphi_i, \quad (\text{B-7})$$

and

$$RR = \sum_i F^2(\tau_i, D_i, H_i) \cos^2(\varphi_i - \theta). \quad (\text{B-8})$$

The computation of the coherence requires the averaging of sequential terms of the form of Eqs. (B-6), (B-7), and (B-8). The average is taken over all of the random variables in the terms. Thus, the averaging amounts to converting the summation to an integral over τ_i , D_i , H_i , and φ_i . The equation for the coherence can be written

$$|\text{coh}(XR)| = \frac{\int F^2 d\tau dD dH \int_0^{2\pi} \cos \varphi \cos(\varphi - \theta) d\varphi}{\left[\int F^2 d\tau dD dH \int_0^{2\pi} \cos^2 \varphi d\varphi \right]^{1/2} \left[\int F^2 d\tau dD dH \int_0^{2\pi} \cos^2(\varphi - \theta) d\varphi \right]^{1/2}}. \quad (\text{B-9})$$

The integrations over τ , D , and H produce terms that cancel in the numerator and denominator; there remains

$$|\text{coh}(XR)| = \frac{\int_0^{2\pi} \cos \varphi \cos(\varphi - \theta) d\varphi}{\left[\int_0^{2\pi} \cos^2 \varphi d\varphi \right]^{1/2} \left[\int_0^{2\pi} \cos^2(\varphi - \theta) d\varphi \right]^{1/2}} \quad (\text{B-10})$$

Performing the integrations yields

$$|\text{coh}(XR)| = \cos \theta ,$$

which is Eq. (B-1).

Since we are assuming that there are no decorrelating effects due to geological inhomogeneities (and, by implication, that sensor noise is negligible), Eq. (A-10) implies that

$$|\text{coh}(YR)| = \sin \theta . \quad (\text{B-11})$$

Then, substituting Eqs. (B-1), (B-11), and the definition $|\gamma_{XY}| = |\text{coh}(XY)|$ into Eqs. (8) and (9) yields

$$A = \frac{\cos \theta - |\gamma_{XY}| \sin \theta}{1 - \gamma_{XY}^2} \quad (\text{B-12})$$

and

$$|B| = \frac{\sin \theta - |\gamma_{XY}| \cos \theta}{1 - \gamma_{XY}^2} \quad (\text{B-13})$$

DINGER AND GOLDSTEIN

These are the desired equations. In this report values of A and B are determined from the recorded data and then used to calculate θ . For this purpose, Eqs. (B-12) and (B-13) are solved for $\sin \theta$ and $\cos \theta$ respectively:

$$\sin \theta = \frac{(\gamma_{XY}^2 - 1)\gamma_{XY}A \pm [2\gamma_{XY}^2(1 - \gamma_{XY}^2) + \gamma_{XY}^4(\gamma_{XY}^2 + A^2) - A^2 + 1]^{1/2}}{1 + \gamma_{XY}^2}, \quad (\text{B-14})$$

and

$$\cos \theta = \frac{(\gamma_{XY}^2 - 1)\gamma_{XY}B \pm [2\gamma_{XY}^2(1 - \gamma_{XY}^2) + \gamma_{XY}^4(\gamma_{XY}^2 + B^2) - B^2 + 1]^{1/2}}{1 + \gamma_{XY}^2} \quad (\text{B-15})$$